Journal of Micro-Bio Robotics
https://doi.org/10.1007/s12213-021-00141-y

RESEARCH ARTICLE

Centipede bio-extremity elastic model control

Joel Miranda Guaderrama[1] · Edgar Alonso Martínez-García[1]

Received: 29 April 2020 / Revised: 12 July 2020 / Accepted: 4 January 2021

Abstract
In this research, a specimen of arthropod, infraspecies *Cormocephalus calcaratus* (centipede) is the matter of study for modeling its trunk-limb biomechanics. The endoskeletal system was built to model and approach its passive dynamics motion. The limb's musculoskeletal system was digitally 'sculpted' in three-dimension using the planar taxonomic sagittal, ventral and transventral views as metrical references, constrained in scale and geometry. The endoskeleton was modeled by an equivalent network of spring-mass-damper muscles with five joints controlled by two input muscles to manipulate the limb's tip. The kinematic position equations with their higher-order derivatives and the inner muscles dynamics were deduced for a Newton-based dynamic controller to resemble scramble up motion. Simulations produced realistic controlled motions with expected limb's dexterity underactuation.

Keywords Biorobot · Centipede · Underactuation · Limb · Musculoskeletal dexterity · 3D modeling

1 Introduction

In the last years, research on biological species have inspired robotics engineering towards enhancing and developing both, intelligence and locomotion for modern robotic technology [1]. The advantages obtained from bioinspired designs are less conservative effectors with fluent motions controlled by their own natural physics-based models. This study is motivated by the need to understand the highly efficient nature of insects. The role of biorobotics in modern technological development is becoming a global inspiration taken from numerous biological species. For instance, robotic fish have emulated the efficiency of biological fish's exoskeleton that yields fluent and highly effective swimming motions [2, 3]. Some underwater bioinspired robots such as octopus-like [4, 5] and manta-like [6] have been developed using soft materials to accomplish agile wavy locomotion and dexterous maneuvers spending very low mechanical energy. Amphibious robots' limb exert hybrid motion, either terrestrial walking or underwater swimming [7]. Robotic lizards [8–10] and snake robots [11, 12] have proven amazing crawling skills deploying low energy locomotion costs. Robotic birds exhibit prominent maneuverability of flapping flight despite changes in aerodynamic forces, reaching precise high-frequency performance of instantaneous wing trajectory tracking [13]. Perhaps, the largest number of studies reported in biorobotics are on arachnid robots [14], where multi-legged robots are redundantly hyper-static, often highly dexterous terrestrial walkers [15]. The study disclosed in this work focuses on the massive multi-legged biomechanics exhibited by centipedes [16–18].

The study of insect's limbs and their capability to move, jump, climb, hunt, scramble up and predate represents a research field of relevance in biorobotics. The *Chilopoda* class of the *phylum arthropoda* has an anatomy that provides particular biomechanical advantages, such as being capable to climb over virtually any surface. The *subphylum myriapoda* contains organisms such as the millipedes (*Diplopoda*) and centipedes (*Chilopoda*), which range from fourteen to forty eight pairs of legs. The centipede insect dexterity changes from specie to specie due to size, number of segments and morphology exhibiting a wide range of sizes. The smallest ones hunt bugs, while the biggest ones catch up to little birds and rodents. The *Scolopendromorpha* order has the biggest specimen

✉ Edgar Alonso Martínez-García
edmartin@uacj.mx

Joel Miranda Guaderrama
migujoel@mail.com

[1] Laboratorio de Robótica, Institute of Engineering and Technology, Universidad Autónoma de Ciudad Juárez, Ciudad Juárez, Mexico

of centipede. The centipede is by nature symmetrically body segmented (Fig. 1a) exhibiting external simplicity. Endoskeletal tendons of head and trunk are ordered by pairs of tendons arranged by segments to support the dorsal, lateral and *sternum*'s longitudinal muscles. The *Chilopoda*'s morphology such as the body's length, the longitudinal alignment of the trunk segments and the absence of articulated inter-segments are due to elasticity of the *sclerite cuticle* and the form of intersegmental joints. The lateral flexibility of the trunk is enhanced by the presence of intercalated *sternites*. The intercalary sternites and tergites in the *geophilomorpha* facilitate strong shortening of the body used during burrowing. Simple longitudinal hinge lines in *Scolopendromorpha* facilitate flattening of a segment and its reverse.

Arthropods are one of the biggest *phylum*, their hunting success comes from the advantages of having numerous legs. Therefore, the number of legs attracts the attention

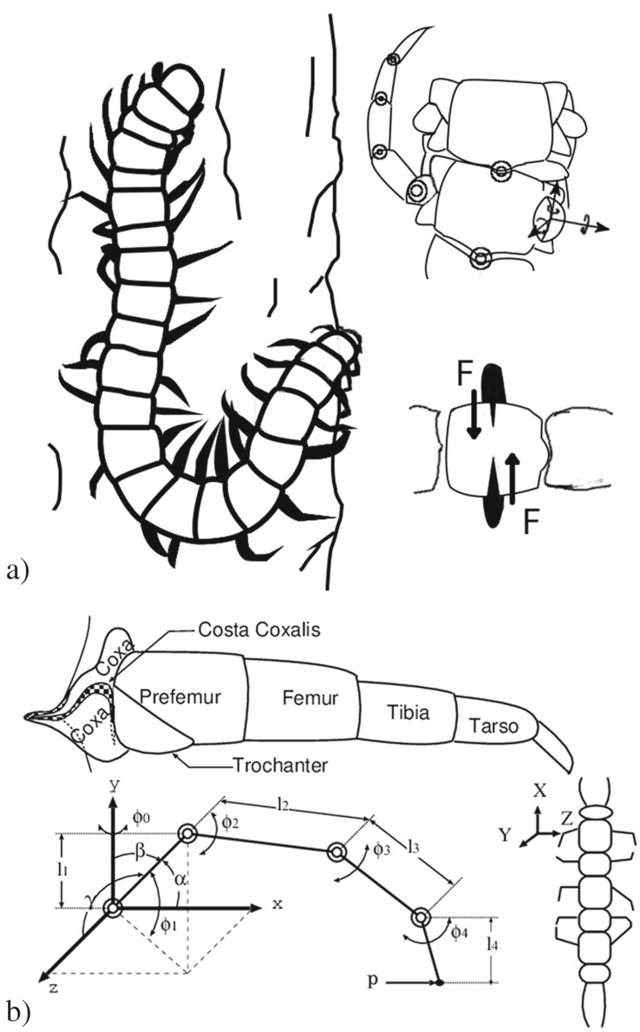

Fig. 1 Centipede anatomy. **a** *Chilopod*'s morphology. **b** Limb's kinematic (angles ϕ_i, α, β, γ and lenghts l_i)

for biological inspiration to design highly dexterous robots. Across the different *subphylums* species, their great maneuverability and dexterity basically solves locomotion for almost any terrain. During this study, the nearest morphological reference found of an *scolopendromorpha* was the *Cormocephalus calcaratus*, belonging to the same subclass. These species have longer links (Fig. 1b) than other species of similar type, thus its metrical scales simplified this study. The *Chilopoda*'s large number of legs allows high tolerance to errors against falls or instability [24, 25], when amputated legs, the specimen is capable to walk and climb preserving maneuverability. The larger the number of legs, the better hyper-static stability is yielded and higher complex dexterity, consequently. The limb's biomechanics is compounded by networks of bio-elastic systems that provide high dexterity and compliance. Understanding the complexity of multi-legged insects endoskeleton is fundamental to model and design highly efficient artificial bioinspired machines. The work [24] researched on a centipede-like robot with twelve legs and six body segments passively connected through yaw joints of torsional springs. Stability and maneuverability in locomotion were quantitatively investigated. The work in [21], reported a muscle-based control method to simulate three-dimension walking biped creatures. Muscle routing and parameters optimization resulted in actuation forces that generated torque patterns incorporating biomechanical constraints, finding different gaits and target speed of generic locomotion. In [22], a footing control of a trunk-segmented centipede-like robot with modular pair of legs conceptualized gaits of the fore limbs' tip being followed by the rear limbs. In [23], a six-legged robot with abstracted anatomy of the insect's leg mechanism was reported. The leg's proportions and muscles were studied to yield motion using bioinspired spring-based passive compliance for the leg's distal segment to soften foot impacts (Fig. 2).

The following Table 1 shows some taxonomic and anatomic features of the biological specimen, which was taken as a matter of study in this manuscript.

The purpose of this work is to build an endoskeletal *coxa*-limb computational model to deduce its motion dynamics for numerical simulation, such as the elastic properties of muscular extension, contraction and joints rotation. The present work's contributions are: **1)** An original three-dimension (3D) endoskeleton model by computer assisted design (CAD) of an *Arthropod*'s limb "sculpted" from assembling the sagittal, ventral, and transversal taxonomic planes (metric references). The endoskeleton network was characterized by a set of sliding vectors. The "sculpted" model reduced the muscles network but resembled equivalent passive dynamics. **2)** Deduction of the kinematics and passive dynamics of the limb and endoskeleton network. A variant of the Hill's model was

Fig. 2 *Scolopendra Calcaratus* (Photos from [24])

established using distal segments that combine over and critically damped muscles. **3)** Reduction of the endoskeletal network into an equivalent three-muscle bifurcation model, two inputs one output governed by underactuated dynamic laws. **4)** A customized biomechanical controller including forward and backward dynamic solutions. Solving the lengths of the input muscles knowing a desired position and solving force/torque in terms of desired limb's speed.

In this paper, Section 2 describes the technique used to "sculpt" the *coxa*-limb 3D musculoskeletal model. Section 3 deduces the high-order kinematics to describe the limb's dexterity. Section 4 mathematically models the endoskeletal network passive dynamics. Section 5 describes the biomechanical dynamic controller. Finally, Section 7 discusses the work's conclusion.

2 Taxonomic 3D "sculpting"

Reproducing the inside *Chilopod*'s limb biomechanics using as reference a real biological specimen may result too difficult to carry out due to its endoskeletal network millimeter scale. Available from entomologists, the taxonomic views are accurate resources that map positions, forms and

Table 1 Centipede's biological features

Scientific classification			
Kingdom:	*Animalia*	Order:	*Scolopendromorpha*
Phylum:	*Arthropoda*	Family:	*Scolopendridae*
Subphylum:	*Myriapoda*	Genus:	*Scolopendra*
Class:	*Chilopoda*	Species:	*S. calcaratus*
Anatomic features			
Segments	21 - 23	Width	15.24 mm
Limb's links	4	Length	150 mm
Limb size	5.1328 mm		

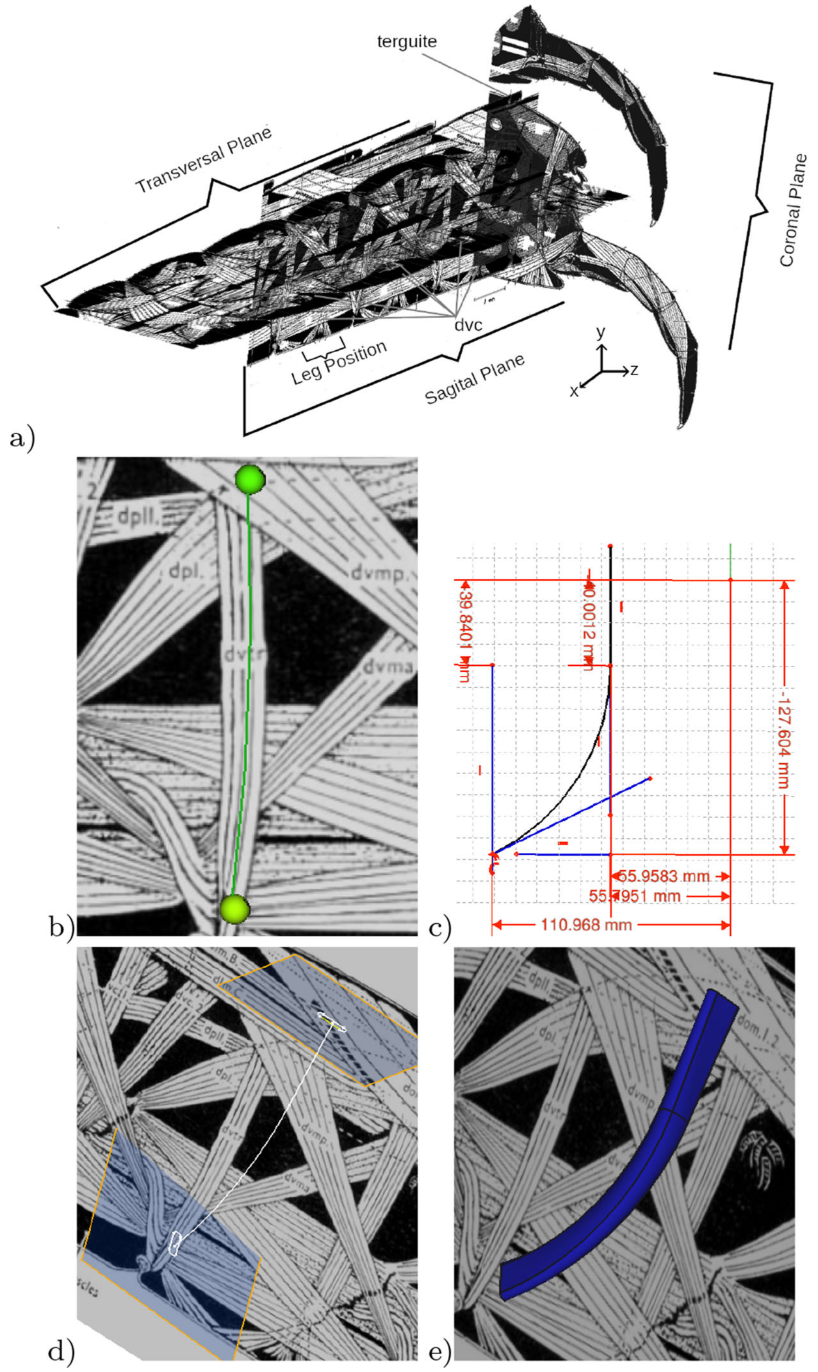

Fig. 3 Endoskeletal CAD-model construction. **a** Taxonomic planes coupling; **b** muscle's Cartesian points; **c** metric outlining; **d** points fitting; **e** muscle shaping

geometrical metric proportions (Fig. 3a). The *chilopoda* taxonomic maps and notation developed in the present work were taken from [26] for the "sculpting" process (Fig. 3bcde). The method developed in this work to realistically "sculpt" the *coxa*-limb endoskeletal network was the use of a CAD software to map muscles and tendons. The reference map was an orthogonal coupling of the planar taxonomical views: sagittal, coronal and transventral (Fig. 3a), which provided accurate sizes and metric geometric proportions. For instance, Fig. 3b shows a pair of 3D points outlining the *dvtr* muscle. The start and end points of a sliding vector are set through the Cartesian taxonomic planes to compound vectored tendons and muscles, forming curved lines as depicted in Fig. 3c. The vectored muscles are projected over the orthogonal planes connecting key-points as shown in Fig. 3d. The muscles shaping were profiled through numerical interpolations, resulting in numerous vectors that assembled the muscles connection between the body-coxa and the *coxa*-limb. One of the contributions of this work is the resulting endoskeletal system characterized by a set of spatial vectors that numerically models the limb's biomechanics. Therefore, the limb's kinematic of motion and its passive dynamics have realistically been simulated. This approach calculated the Cartesian vectors shown in Appendix A, the muscles' length in Appendix B, the muscles unit vectors provided in Appendix C and the list of direction cosines in Appendix D.

For instance, the size and thickness of the muscle *dvtr* (Fig. 3e) was taken as a key reference. *dvtr*'s thickness and size allowed to estimate other muscles' thickness and size by using metric proportions. Besides, *dvtr* functioned as a common geometric reference for Cartesian planes alignment because this muscle is a crossover. Figure 4a depicts the whole endoskeletal CAD model built. Different colors easy visual identification for the reader. Chosen colors classify in accordance to the type of muscles' function such as stabilizers, rotators, retractors and protractors (see Fig. 4c and Appendix E).

From a biorobotics approach, an interest of this work is to exploit the natural limb's biomechanical underactuation. This work considered understanding the passive dynamics of a pair of muscles as independent linear inputs to control the limb's position, speed and applied forces, namely *lev.tr.a* and *lev.tr.b*. Both input muscles are depicted in the ventral view of Fig. 4b. Moreover, for instance, the capability of shortening and elongation exhibited by *chilopodans* is in particular given by the group of muscles *ret* and the group *pr* (sagittal view of Fig. 4ab and Appendix B). In addition, the ability to perform leg's speedy backstroke and power of reversible dorsoventral flattening are concerned with the group of muscles *dvc* and *tep.tcx* (see Fig. 4b and Appendix E). Furthermore, the *coxa* disposition is controlled by *coxa*-body muscles *co.fe* and the *coxa-trochanter* joints located between femur and *coxa* (Fig. 4b). Each muscle *dvc* intersects the *costa coxalis* allowing rotation around the limb's axis promoting maximum strides and thrust against the ground at all phases of a backstroke.

There are two coxal movements in *Chilopoda*: (i) the normal arthropodan promotor-remotor swing; and (ii) the rotation of the leg on its long axis, resulting from the parasagittal *rock*[1] of the *coxa* about a more or less ventral *fulcrum*.

In this work, the reconstructed network of muscles meet equivalence with an over damped system of elastic elements (see Appendix A), where each muscle is modeled by an equivalent variation of the Hill's model [28], subsequently discussed in Section 4. Given the endoskeletal network heteronomy such as sclerites, muscles and joints, the limb's biomechanics provides stability at the leg-bearing segment. Biomechanical stability reduces the limb's lateral undulations particularly by the group of elements *co.fe* and

[1]Study of *rock-coxa* are further described in [27] pp.73.

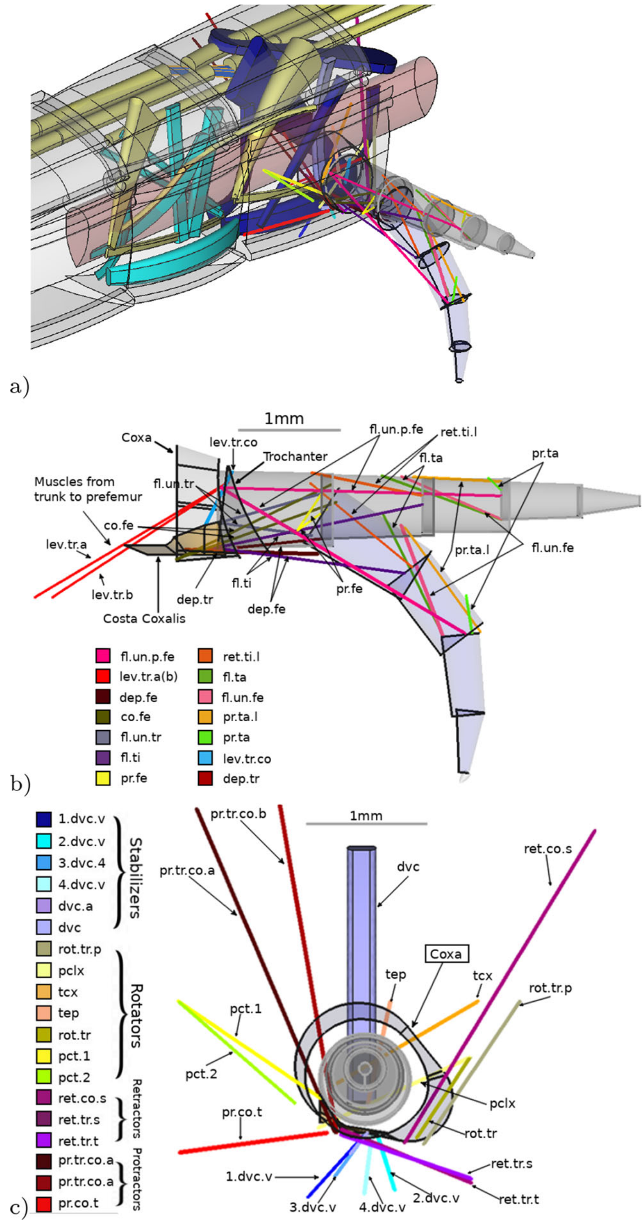

Fig. 4 Computer-based biomechanical endoskeleton. a) Network of muscles and tendons, *rock-coxa*-limb; b) ventral-view; and c) sagital-view

lev.tr.co and muscles layouts (Appendixes C and D). The trunk segmental tendons and muscles (*anamorpha*) improve performance of *anamorphic* walking patterns, exhibiting uniformity in their origins from the ventral segmental tendons, intersegment or limb bases. Thus, establishing a coordinate system to represent motion is fundamental. Cartesian starting locations (nearest to the *coxa*) of branches of ventral segmental tendons, intersegment and limb bases were numerically averaged to obtain a general spatial origin. However, the origin as well as minimum and maximum locations resulted out of phase w.r.t. the *coxa*'s center.

Nevertheless, it was found out that the surface of a spherical model made a coarse "best fit" to the muscles positions. Therefore, a spherical joint model fitted trunk-limb with *coxa*'s center (Fig. 5). Using the CAD endoskeleton, numerical parameters of muscles were obtained. Let us define the k^{th} general element basic vector points. The start and end points of a muscle are respectively $\mathbf{q}_k, \mathbf{r}_k \in \mathbb{R}^3$, such that $\mathbf{q}_k, \mathbf{r}_k = (x, y, z)^\top$, with elements length

$$\mathbf{u}_k = \sqrt[2]{(\mathbf{r}_x - \mathbf{q}_x)^2 + (\mathbf{r}_y - \mathbf{q}_y)^2 + (\mathbf{r}_z - \mathbf{q}_z)^2}, \tag{1}$$

with each element's direction angles α_k, β_k and γ_k defined by the general expression:

$$\begin{pmatrix} \alpha_k \\ \beta_k \\ \gamma_k \end{pmatrix} = \arccos\left(\frac{\mathbf{r}_k - \mathbf{q}_k}{\|\mathbf{u}_k\|}\right). \tag{2}$$

Calculations of geometric parameters of *coxa*-limb muscles were estimated and are shown in Appendixes A to E. Further analytic models are deduced in Section 4.

3 Limb Dexterity Model

In accordance to the limb elements with five rotary joints that is depicted in free-body diagram of Fig. 1b, this section deduces the limb's kinematic model to describe its geometry of motion. Deduction of the limb's tip Cartesian position is of interest in this work. Subsequently, higher-order derivatives of kinematics are obtained as fundamentals for the passive dynamic model. The expression Eq. 3 describes the lim's tip position $\mathbf{p}$, given the joints angles (denoted by ϕ_{01234}). The model $\mathbf{p}$ is a Cartesian vector, where $\mathbf{p} \in \mathbb{R}^3$, such that $\mathbf{p} = (x, y, z)^\top$. Thus,

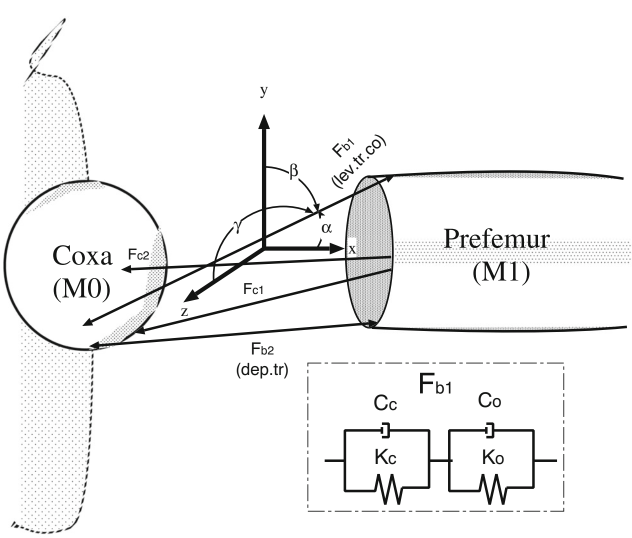

Fig. 5 View of spherical joint and the muscle model

$$\mathbf{p} = \begin{pmatrix} l_1 \sin(\phi_0)\cos(\phi_1) + l_2 \sin(\phi_0)\cos(\phi_1+\phi_2) + \\ l_3 \sin(\phi_0)\cos(\phi_1+\phi_2+\phi_3) + \\ l_4 \sin(\phi_0)\cos(\phi_1+\phi_2+\phi_3+\phi_4) \\ \\ l_1 \sin(\phi_1) + l_2 \sin(\phi_1+\phi_2) + \\ l_3 \sin(\phi_1+\phi_2+\phi_3) + \\ l_4 \sin(\phi_1+\phi_2+\phi_3+\phi_4) \\ \\ l_1 \cos(\phi_0)\cos(\phi_1) + l_2 \cos(\phi_0)\cos(\phi_1+\phi_2) + \\ l_3 \cos(\phi_0)\cos(\phi_1+\phi_2+\phi_3) + \\ l_4 \cos(\phi_0)\cos(\phi_1+\phi_2+\phi_3+\phi_4) \end{pmatrix}. \tag{3}$$

Deriving with respect to (w.r.t.) time previous expression Eq. 3, the higher-order derivative is obtained, being a time-variant linear model of the form $\dot{\mathbf{p}} = \mathbf{J} \cdot \dot{\mathbf{\Phi}}$. Where the non-squared matrix $\mathbf{J}$ is the Jacobian and represents how the limb's position changes w.r.t. the rate of rotation of all joints simultaneously. The vector $\mathbf{\Phi} \in \mathbb{R}^5$, $\dot{\mathbf{\Phi}} = (\dot{\phi}_0, \dot{\phi}_1, \dot{\phi}_2, \dot{\phi}_3, \dot{\phi}_4)^\top$ is the vector of independent control variables of the limb's rotary joints. Thus, hereafter for the purpose of shortening too long trigonometric expressions, particularly obtained from higher-order derivatives, let us define the following notation in Definition 1.

Definition 1 (sin, cos short notation) Let the function sine be re-defined as s, and let the function cosine be re-defined as c. Such that, with parameters ϕ_m, ϕ_n, the equivalent reduced notation is:

$$\mathrm{s}_m + \mathrm{c}_{mn} \equiv \sin(\phi_m) + \cos(\phi_m + \phi_n)$$

Thus, previous Definition 1 is to be used into the next higher-order derivative expressions. The Cartesian limb's speed model describes the rate of change of the limb's tip for the x component as

$$\begin{aligned} \dot{x} =& (l_1\mathrm{c}_0\mathrm{c}_1 + l_2\mathrm{c}_0\mathrm{c}_{12} + l_3\mathrm{c}_0\mathrm{c}_{123} + l_4\mathrm{c}_0\mathrm{c}_{1234})\dot{\phi}_0 \\ &- (l_1\mathrm{s}_0\mathrm{s}_1 + l_2\mathrm{s}_0\mathrm{s}_{12} + l_3\mathrm{s}_0\mathrm{s}_{123} + l_4\mathrm{s}_0\mathrm{s}_{1234})\dot{\phi}_1 \\ &- (l_2\mathrm{s}_0\mathrm{s}_{12} + l_3\mathrm{s}_0\mathrm{s}_{123} + l_4\mathrm{s}_0\mathrm{s}_{1234})\dot{\phi}_2 - (l_3\mathrm{s}_0\mathrm{s}_{123} \\ &+ l_4\mathrm{s}_0\mathrm{s}_{1234})\dot{\phi}_3 - l_4\mathrm{s}_0\mathrm{s}_{1234}\dot{\phi}_4, \end{aligned} \tag{4}$$

similarly, the speed rate of change along the y component,

$$\begin{aligned} \dot{y} =& (l_1\mathrm{c}_1 + l_2\mathrm{c}_{12} + l_3\mathrm{c}_{123} + l_4\mathrm{c}_{1234})\dot{\phi}_1 \\ &+ (l_2\mathrm{c}_{12} + l_3\mathrm{c}_{123} + l_4\mathrm{c}_{1234})\dot{\phi}_2 \\ &+ (l_3\mathrm{c}_{123} + l_4\mathrm{c}_{1234})\dot{\phi}_3 + l_4\mathrm{c}_{1234}\dot{\phi}_4, \end{aligned} \tag{5}$$

likewise, the speed motion along the z component:

$$\begin{aligned} \dot{z} =& -(l_1\mathrm{s}_0\mathrm{c}_1 + l_2\mathrm{s}_0\mathrm{c}_{12} + l_3\mathrm{s}_0\mathrm{c}_{123} + l_4\mathrm{s}_0\mathrm{c}_{1234})\dot{\phi}_0 \\ &- (l_1\mathrm{c}_0\mathrm{s}_1 + l_2\mathrm{c}_0\mathrm{s}_{12} + l_3\mathrm{c}_0\mathrm{s}_{123} + l_4\mathrm{c}_0\mathrm{s}_{1234})\dot{\phi}_1 \\ &- (l_2\mathrm{c}_0\mathrm{s}_{12} + l_3\mathrm{c}_0\mathrm{s}_{123} + l_4\mathrm{c}_0\mathrm{s}_{1234})\dot{\phi}_2 \\ &- (l_3\mathrm{c}_0\mathrm{s}_{123} + l_4\mathrm{c}_0\mathrm{s}_{1234})\dot{\phi}_3 - l_4\mathrm{c}_0\mathrm{s}_{1234}\dot{\phi}_4. \end{aligned} \tag{6}$$

Moreover, by obtaining the Jacobian matrix elements in terms of the joints rotary angles, the following terms are related to the x component:

$$\frac{\partial\phi_0}{\partial x} = c_0 \sum_{i=1}^{4} l_i \cos\left(\sum_{j=1}^{i}\phi_j\right); \ \frac{\partial\phi_1}{\partial x} = -s_0 \sum_{i=1}^{4} l_i \sin\left(\sum_{j=1}^{i}\phi_j\right);$$
$$\frac{\partial\phi_2}{\partial x} = -s_0 \sum_{i=2}^{4} l_i \sin\left(\sum_{j=1}^{i}\phi_j\right); \ \frac{\partial\phi_3}{\partial x} = -s_0 \sum_{i=3}^{4} l_i \sin\left(\sum_{j=1}^{i}\phi_j\right);$$
$$\frac{\partial\phi_4}{\partial x} = -l_4 s_0 \sin\left(\sum_{j=1}^{i}\phi_j\right).$$

In addition, the Jacobian matrix elements that represent the y Cartesian component are,

$$\frac{\partial\phi_0}{\partial y} = 0; \ \frac{\partial\phi_1}{\partial y} = \sum_{i=1}^{4} l_i \cos\left(\sum_{j=1}^{i}\phi_j\right); \ \frac{\partial\phi_2}{\partial y} = \sum_{i=3}^{4} l_i \cos\left(\sum_{j=1}^{i}\phi_j\right);$$
$$\frac{\partial\phi_3}{\partial y} = -s_0 \sum_{i=3}^{4} l_i \sin\left(\sum_{j=1}^{i}\phi_j\right); \ \frac{\partial\phi_4}{\partial y} = l_4 \cos\left(\sum_{j=1}^{4}\phi_j\right).$$

Finally, the Jacobian matrix elements that represent the z Cartesian component are,

$$\frac{\partial\phi_0}{\partial x} = -s_0 \sum_{i=1}^{4} l_i \cos\left(\sum_{j=1}^{i}\phi_j\right); \ \frac{\partial\phi_1}{\partial x} = -c_0 \sum_{i=1}^{4} l_i \sin\left(\sum_{j=1}^{i}\phi_j\right);$$
$$\frac{\partial\phi_2}{\partial x} = -c_0 \sum_{i=2}^{4} l_i \sin\left(\sum_{j=1}^{i}\phi_j\right); \ \frac{\partial\phi_3}{\partial x} = -c_0 \sum_{i=3}^{4} l_i \sin\left(\sum_{j=1}^{i}\phi_j\right);$$
$$\frac{\partial\phi_4}{\partial x} = -l_4 c_0 \sin\left(\sum_{j=1}^{i}\phi_j\right).$$

Therefore, the Jacobian matrix form is fulfilled with the partial differential terms as the following expression,

$$\mathbf{J} = \begin{pmatrix} \frac{\partial\phi_0}{\partial x} & \frac{\partial\phi_1}{\partial x} & \frac{\partial\phi_2}{\partial x} & \frac{\partial\phi_3}{\partial x} & \frac{\partial\phi_4}{\partial x} \\ 0 & \frac{\partial\phi_1}{\partial y} & \frac{\partial\phi_2}{\partial y} & \frac{\partial\phi_3}{\partial y} & \frac{\partial\phi_4}{\partial y} \\ \frac{\partial\phi_0}{\partial z} & \frac{\partial\phi_1}{\partial z} & \frac{\partial\phi_2}{\partial z} & \frac{\partial\phi_3}{\partial z} & \frac{\partial\phi_4}{\partial z} \end{pmatrix}. \tag{7}$$

Therefore, in order to obtain the second-order derivative model, let us derive the fundamental time-variant linear function $\dot{\mathbf{p}} = \mathbf{J}\cdot\dot{\mathbf{\Phi}}$, such that

$$\ddot{\mathbf{p}} = \dot{\mathbf{J}}\cdot\dot{\mathbf{\Phi}} + \mathbf{J}\cdot\ddot{\mathbf{\Phi}}, \tag{8}$$

then, by algebraically expanding previous model with separated derivation of Cartesian components w.r.t. time, let us obtain the expressions Eqs. 4, 5 and 6.

Thus, the acceleration model $\ddot{x}$ is algebraically expanded and shown separately,

$$\begin{aligned}\ddot{x} =& (l_1 c_0 c_1 + l_2 c_0 c_{12} + l_3 c_0 c_{123} + l_4 c_0 c_{1234})\ddot{\phi}_0 - \\ & (l_1 s_0 s_1 + l_2 s_0 s_{12} + l_3 s_0 s_{123} + l_4 s_0 s_{1234})\ddot{\phi}_1 - \\ & (l_2 s_0 s_{12} + l_3 s_0 s_{123} + l_4 s_0 s_{1234})\ddot{\phi}_2 - \\ & (l_3 s_0 s_{123} + l_4 s_0 s_{1234})\ddot{\phi}_3 - l_4 s_0 s_{1234}\ddot{\phi}_4 - \\ & (l_1 s_0 c_1 + l_2 s_0 c_{12} + l_3 s_0 c_{123} + l_4 s_0 c_{1234})\dot{\phi}_0^2 - \\ & (l_1 s_0 c_1 + l_2 s_0 s_{12} + l_3 s_0 s_{123} + l_4 s_0 s_{1234})\dot{\phi}_1^2 - \\ & (l_2 s_0 c_{12} + l_3 s_0 c_{123} + l_4 s_0 c_{1234})\dot{\phi}_2^2 - \\ & (l_3 s_0 c_{123} + L_4 s_0 c_{1234})\dot{\phi}_3^2 - l_4 s_0 c_{1234}\dot{\phi}_4^2 - \\ & (l_1 c_0 s_1 + l_2 c_0 s_{12}\dot{\phi}_1 + l_2 c_0 s_{12}\dot{\phi}_2 + l_3 c_0 s_{123}\dot{\phi}_1 + \\ & l_3 c_0 s_{123}\dot{\phi}_2 + l_3 c_0 s_{123}\dot{\phi}_3 + l_4 c_0 s_{1234}\dot{\phi}_1 + l_4 c_0 s_{1234}\dot{\phi}_2 + \\ & l_4 c_0 s_{1234}\dot{\phi}_3 + l_4 c_0 s_{1234}\dot{\phi}_4)\dot{\phi}_0 - (l_1 c_0 s_1 \dot{\phi}_0 + \\ & l_2 c_0 s_{12}\dot{\phi}_0 + l_2 s_0 c_{12}\dot{\phi}_2 + l_3 c_0 s_{123}\dot{\phi}_0 + l_3 s_0 c_{123}\dot{\phi}_2 + \\ & l_3 s_0 c_{123}\dot{\phi}_3 + l_4 c_0 s_{1234}\dot{\phi}_0 + l_4 s_0 c_{1234}\dot{\phi}_2 + \\ & l_4 s_0 c_{1234}\dot{\phi}_3 + l_4 s_0 c_{1234}\dot{\phi}_4)\dot{\phi}_1 - (l_2 c_0 s_{12}\dot{\phi}_0 + \\ & l_2 s_0 c_{12}\dot{\phi}_1 + l_3 c_0 s_{123}\dot{\phi}_0 + l_3 s_0 c_{123}\dot{\phi}_1 + \\ & l_3 s_0 c_{123}\dot{\phi}_3 + l_4 c_0 s_{1234}\dot{\phi}_0 + l_4 s_0 c_{1234}\dot{\phi}_1 + \\ & l_4 s_0 c_{1234}\dot{\phi}_3 + l_4 s_0 c_{1234}\dot{\phi}_4)\dot{\phi}_2 - (l_3 c_0 s_{123}\dot{\phi}_0 + \\ & l_3 s_0 c_{123}\dot{\phi}_1 + l_3 s_0 c_{123}\dot{\phi}_2 + l_4 c_0 s_{1234}\dot{\phi}_0 + \\ & l_4 s_0 c_{1234}\dot{\phi}_1 + l_4 s_0 c_{1234}\dot{\phi}_2 + l_4 s_0 c_{1234}\dot{\phi}_4)\dot{\phi}_3 - \\ & (l_4 c_0 s_{1234}\dot{\phi}_0 + l_4 s_0 c_{1234}\dot{\phi}_1 + l_4 s_0 c_{1234}\dot{\phi}_2 + \\ & l_4 s_0 c_{1234}\dot{\phi}_3)\dot{\phi}_4.\end{aligned} \tag{9}$$

Similarly, the acceleration model $\ddot{y}$ is algebraically expanded and shown separately,

$$\begin{aligned}\ddot{y} =& (l_1 c_1 + l_2 c_{12} + l_3 c_{123} + l_4 c_{1234})\ddot{\phi}_1 + \\ & (l_2 c_{12} + l_3 c_{123} l_4 c_{1234})\ddot{\phi}_2 + (l_3 c_{123} + \\ & l_4 c_{1234})\ddot{\phi}_3 + l_4 c_{1234}\ddot{\phi}_4 - \\ & (l_1 s_1 + l_2 s_{12} + l_3 s_{123} + l_4 s_{1234})\dot{\phi}_1^2 + \\ & (l_2 s_{12} + l_3 s_{123} + l_4 s_{1234})\dot{\phi}_2^2 + \\ & (l_3 s_{123} + l_4 s_{1234})\dot{\phi}_3^2 + l_4 s_{1234}\dot{\phi}_4^2 - (l_2 s_{12}\dot{\phi}_2 + \\ & l_3 s_{123}\dot{\phi}_2 + l_3 s_{123}\dot{\phi}_3 + l_4 s_{1234}\dot{\phi}_2 + l_4 s_{1234}\dot{\phi}_3 + \\ & l_4 s_{1234}\dot{\phi}_4)\dot{\phi}_1 - (l_2 s_{12}\dot{\phi}_1 + \\ & l_3 s_{123}\dot{\phi}_1 + l_3 s_{123}\dot{\phi}_3 + l_4 s_{1234}\dot{\phi}_1 + l_4 s_{1234}\dot{\phi}_3 + \\ & l_4 s_{1234}\dot{\phi}_4)\dot{\phi}_2 - (l_3 s_{123}\dot{\phi}_1 + l_3 s_{123}\dot{\phi}_2 + l_4 s_{1234}\dot{\phi}_1 + \\ & l_4 s_{1234}\dot{\phi}_2 + l_4 s_{1234}\dot{\phi}_4)\dot{\phi}_3 + (l_4 s_{1234}\dot{\phi}_1 + \\ & l_4 s_{1234}\dot{\phi}_2 + l_4 s_{1234}\dot{\phi}_3)\dot{\phi}_4.\end{aligned} \tag{10}$$

Likewise, the acceleration model $\ddot{z}$ is algebraically expanded and shown separately,

$$
\begin{aligned}
\ddot{z} = {} & (l_1 s_0 c_1 + l_2 s_0 c_{12} + l_3 s_0 c_{123} - l_4 s_0 c_{1234})\ddot{\phi}_0 - \\
& (l_1 c_0 s_1 + l_2 c_0 s_{12} + l_3 c_0 s_{123} + l_4 c_0 s_{1234})\ddot{\phi}_1 - \\
& (l_2 c_0 s_{12} + l_3 c_0 s_{123} + l_4 c_0 s_{1234})\ddot{\phi}_2 - \\
& (l_3 c_0 s_{123} + l_4 c_0 s_{1234})\ddot{\phi}_3 - l_4 c_0 s_{1234}\ddot{\phi}_4 - \\
& (l_1 c_0 s_1 + l_2 c_0 c_{12} + l_3 c_0 c_{123} + l_4 c_0 c_{1234})\dot{\phi}_0^2 - \\
& (l_1 c_0 c_1 + l_2 c_0 c_{12} + l_3 c_0 c_{123} + l_4 c_0 c_{1234})\dot{\phi}_1^2 - \\
& (l_2 c_0 c_{12} + l_3 c_0 c_{123} + l_4 c_0 c_{1234})\dot{\phi}_2^2 - \\
& (l_3 c_0 c_{123} + L_4 c_0 c_{1234})\dot{\phi}_3^2 - l_4 c_0 c_{1234}\dot{\phi}_4^2 - \\
& (l_1 s_0 s_1 + l_2 s_0 s_{12}\dot{\phi}_1 + l_2 s_0 s_{12}\phi_2 + l_3 s_0 s_{123}\dot{\phi}_1 + \\
& l_3 s_0 s_{123}\dot{\phi}_2 + l_3 s_0 s_{123}\dot{\phi}_3 + l_4 s_0 s_{1234}\dot{\phi}_1 + l_4 s_0 s_{1234}\dot{\phi}_2 + \\
& l_4 s_0 s_{1234}\dot{\phi}_3 + l_4 s_0 s_{1234}\dot{\phi}_4)\dot{\phi}_0 + (l_1 s_0 s_1\dot{\phi}_0 + \\
& l_2 s_0 s_{12}\dot{\phi}_0 - l_2 c_0 c_{12}\dot{\phi}_2 + l_3 s_0 s_{123}\dot{\phi}_0 - l_3 c_0 c_{123}\dot{\phi}_2 - \\
& l_3 c_0 c_{123}\dot{\phi}_3 + l_4 s_0 s_{1234}\dot{\phi}_0 - l_4 c_0 c_{1234}\dot{\phi}_2 - \\
& l_4 c_0 c_{1234}\dot{\phi}_3 - l_4 c_0 c_{1234}\dot{\phi}_4)\dot{\phi}_1 + (l_2 s_0 s_{12}\dot{\phi}_0 - \\
& l_2 c_0 c_{12}\dot{\phi}_1 + l_3 s_0 s_{123}\dot{\phi}_0 - l_3 c_0 c_{123}\dot{\phi}_1 - \\
& l_3 c_0 c_{123}\dot{\phi}_3 + l_4 s_0 s_{1234}\dot{\phi}_0 - l_4 c_0 c_{1234}\dot{\phi}_1 - \\
& l_4 c_0 c_{1234}\dot{\phi}_3 - l_4 c_0 c_{1234}\dot{\phi}_4)\dot{\phi}_2 + (l_3 s_0 s_{123}\dot{\phi}_0 - \\
& l_3 c_0 c_{123}\dot{\phi}_1 - l_3 c_0 c_{123}\dot{\phi}_2 + l_4 s_0 s_{1234}\dot{\phi}_0 - \\
& l_4 c_0 c_{1234}\dot{\phi}_1 - l_4 c_0 c_{1234}\dot{\phi}_2 - l_4 c_0 c_{1234}\dot{\phi}_4)\dot{\phi}_3 - \\
& (l_4 s_0 s_{1234}\dot{\phi}_0 - l_4 c_0 c_{1234}\dot{\phi}_1 - l_4 c_0 c_{1234}\dot{\phi}_2 - \\
& l_4 c_0 c_{1234}\dot{\phi}_3)\dot{\phi}_4. \quad (11)
\end{aligned}
$$

By algebraically arranging previous second-order components $\ddot{x}$, $\ddot{y}$ and $\ddot{z}$, the following expression is obtained, which in their matrix forms are equivalent to Eq. 8, thus

$$\ddot{\mathbf{p}} = \mathbf{J} \cdot \ddot{\mathbf{\Phi}} + \mathbf{J}_2 \cdot \dot{\mathbf{\Phi}}^2 + \dot{\mathbf{J}} \cdot \dot{\mathbf{\Phi}}. \quad (12)$$

The expression Eq. 3 represents a forward kinematic solution and is relevant because an inverse analytical solution is non trivial. A method proposed in this work is to obtain a numerical recursive solution by using previous matrix forms, first-order and second-order derivatives.

Therefore, through an algebraic approach the inverse general kinematic solutions for the first and second order are

$$\dot{\mathbf{\Phi}} = \mathbf{J}^+ \cdot \dot{\mathbf{p}} = (\mathbf{J} \cdot \mathbf{J}^\top)^{-1} \cdot \mathbf{J} \cdot \dot{\mathbf{p}}, \quad (13)$$

in these expressions, the Moore-Penrose left-sided pseudoinverse algebraic model is being included in its functional form, since $\mathbf{J}_{m \times n}, \mid m < n$ is non-squared,

$$\ddot{\mathbf{\Phi}} = (\mathbf{J} \cdot \mathbf{J}^\top)^{-1} \cdot \left[\ddot{\mathbf{p}} - \dot{\mathbf{J}} \cdot \dot{\mathbf{\Phi}}\right]. \quad (14)$$

4 Endoskeletal passive dynamic model

This section deduces the endoskeletal passive dynamic model. The geometric elements built into the "sculpted" limb's biomechanics are fundamental to provide a dynamic formulation that is based on the Newton's second-law of motion. In this work, the center of *coxa* has been referenced as the coordinates origin (see Fig. 5). This work proposes a variation of the traditional Hill's muscle composed of spring-mass-damper + spring-mass. The spring-mass element is modified by including a damper element in parallel, as shown in Fig. 5. This change avoids any underdamped effect in the limb when touching the ground or grasping an object. This approach provides the flexibility to configure a muscle by combining over-damped (Co and Ko), critically damped (Cc and Kc) or both mixed. The expression Eq. 15 models cosine directions, being α_k, β_k and γ_k the angles of the k^{th} muscle w.r.t. the axis x, y, z respectively. $\mathbf{r}$ and $\mathbf{q}$ are the begin and end vector points, respectively of an arbitrary muscle. From expressions Eqs. 1- 2 that are related to Fig. 4bc, the direction cosines Appendix D for the k^{th} muscle are

$$
\begin{aligned}
\alpha_k &= \arccos\left(\frac{\mathbf{r}_{x_k} - \mathbf{q}_{x_k}}{\|\mathbf{u}_k\|}\right); \\
\beta_k &= \arccos\left(\frac{\mathbf{r}_{y_k} - \mathbf{q}_{y_k}}{\|\mathbf{u}_k\|}\right); \quad (15) \\
\gamma_k &= \arccos\left(\frac{\mathbf{r}_{z_k} - \mathbf{q}_{z_k}}{\|\mathbf{u}_k\|}\right).
\end{aligned}
$$

The Appendixes A and B collect the real metric values and lengths of the muscles Cartesian components obtained from the computer-generated 3D model.

In addition, the force components in their basic forms are,

$$
\begin{aligned}
fx &= \|\mathbf{f}_k\| \cos(\alpha_k), \\
fy &= \|\mathbf{f}_k\| \cos(\beta_k), \quad (16) \\
fz &= \|\mathbf{f}_k\| \cos(\gamma_k).
\end{aligned}
$$

The resulting limb's general force f_R with center of mass at the *coxa* is a sum of all components

$$f_R = \sqrt[2]{\left(\sum_k \mathrm{f}_{x_k}\right)^2 + \left(\sum_k \mathrm{f}_{y_k}\right)^2 + \left(\sum_k \mathrm{f}_{z_k}\right)^2}. \quad (17)$$

In this work, a slight variation of the Hill's muscle model is proposed. As shown in Fig. 5, a critically damped element is serially coupled with an over-damped one. In this work the traditional Hill's model under damped element is substituted by the critically new spring-mass-damp system in order to dissipate limb's vibrations [29]. As a spring-mass-damper system models a muscle, its general linear elongation is defined by ℓ_k. Thus, the muscle second-order homogeneous differential equation is defined by

$$m_k \ddot{\ell}_k + \mathrm{C}_k \dot{\ell}_k + \mathrm{K}_k \ell_k = 0, \quad (18)$$

where the elastic restitution coefficient is K [kg/s^2]. The damping coefficient is C [kg/s]. The restitution force $m\ddot{\ell}$ counteracts the oscillatory damping effects. The oscillatory velocity and acceleration are denoted by $\dot{\ell}$ and $\ddot{\ell}$ respectively. Thus, solving the 2^{nd}-order differential equation, as a 1^{st}-order equation such that $\mathrm{C}\dot{\ell} = -\mathrm{K}\ell$,

$$\int_\ell \frac{\mathrm{d}\ell}{\ell} = -\frac{\mathrm{K}}{\mathrm{C}} \int_t \mathrm{d}t, \tag{19}$$

hence

$$\ln(\ell) = -\frac{\mathrm{K}}{\mathrm{C}} t + \mathrm{c}, \quad \lambda = -\frac{\mathrm{K}}{\mathrm{C}}, \tag{20}$$

with integration constant $\mathrm{c} = 0$ for analysis purpose. The damping elongation derivatives as functions of time are

$$\ell_d = \mathrm{e}^{\lambda t}, \quad \dot{\ell}_d = \lambda \mathrm{e}^{\lambda t}, \quad \ddot{\ell}_d = \lambda^2 \mathrm{e}^{\lambda t}. \tag{21}$$

Substituting previous expression in Eq. 18,

$$m_k \lambda^2 \mathrm{e}^{\lambda t} + \mathrm{C}_k \lambda \mathrm{e}^{\lambda t} + \mathrm{K}_k \mathrm{e}^{\lambda t} = 0, \tag{22}$$

by algebraically simplifying, the characteristic equation:

$$\lambda^2 + \frac{\mathrm{C}}{m}\lambda + \frac{\mathrm{K}}{m} = 0, \tag{23}$$

Therefore, the following Definition 2 arises:

Definition 2 (**Muscles parameters model**) *The characteristic equation solution is defined by*

$$\lambda_{1,2} = \frac{-\mathrm{C}_k}{2m_k} \pm \frac{\sqrt[2]{\left(\frac{\mathrm{K}_k}{m_k}\right)^2 - 4\frac{\mathrm{K}_k}{m_k}}}{2}. \tag{24}$$

when a critically damped behavior is assumed,

$$\left(\frac{\mathrm{K}}{m}\right)^2 = 4\left(\frac{\mathrm{K}}{m}\right),$$

with one real root defined by

$$\lambda = -\frac{\mathrm{C}}{2m}. \tag{25}$$

The damping motion is analytically solved by

$$\ell_d(t) = W\mathrm{e}^{\lambda t}, \tag{26}$$

with amplitude numeric weight W [m]. When over damped behavior is assumed, analytical solution is defined by

$$\left(\frac{\mathrm{K}_k}{m_k}\right)^2 > 4\left(\frac{\mathrm{K}_k}{m_k}\right).$$

Hereafter, this work discloses the proposed mathematical model that describe the endoskeletal network passive dynamic analysis, which differs from other approaches [30].

After analysis of the muscles network, the proposed general model has fundamentals on

$$\sum_i m_i \ddot{\ell}_i + \sum_j \mathrm{c}_j \dot{\ell}_j + \sum_k \mathrm{k}_k \ell_k = 0.$$

Proposition 1 (***Coxa*** **dynamic model.**) *The dynamic model of muscles for the Coxa is*

$$\begin{aligned} -m_0 \sum_{i=1,3} (\ddot{\ell}_i + \ddot{\ell}_{i+1}) + m_1 \sum_{i=5,7} (\ddot{\ell}_i + \ddot{\ell}_{i+1}) + \\ m_2 \sum_{i=9,11} (\ddot{\ell}_i + \ddot{\ell}_{i+1}) + \sum_{i=1}^{12} (\mathrm{C}_i \dot{\ell}_i + \mathrm{K}_i \ell_i) = 0 \end{aligned} \tag{27}$$

with negative damping coefficient $-\mathrm{C}_3$.

Proposition 2 (***Prefemur*** **dynamic model.**) *The dynamic model of muscles for the Prefemur is*

$$\begin{aligned} -m_0 \sum_{i=5,7} (\ddot{\ell}_i + \ddot{\ell}_{i+1}) + m_2 \sum_{i=19,21} (\ddot{\ell}_i + \ddot{\ell}_{i+1}) + \\ m_3 \sum_{i=15,17} (\ddot{\ell}_i + \ddot{\ell}_{i+1}) - \sum_{i=5}^{8} (\mathrm{C}_i \dot{\ell}_i + \mathrm{K}_i \ell_i) + \\ \sum_{i=13}^{22} (\mathrm{C}_i \dot{\ell}_i + \mathrm{K}_i \ell_i) = 0 \end{aligned} \tag{28}$$

Proposition 3 (***Femur*** **dynamic model.**) *A dynamic model for the Femur*

$$\begin{aligned} -m_0 \sum_{i=9,11} (\ddot{\ell}_i + \ddot{\ell}_{i+1}) - m_1 \sum_{i=19,21} (\ddot{\ell}_i + \ddot{\ell}_{i+1}) + \\ m_4 \sum_{i=27,29} (\ddot{\ell}_i + \ddot{\ell}_{i+1}) - \sum_{i=9}^{12} (\mathrm{C}_i \dot{\ell} + \mathrm{K}_i \ell_i) - \\ \sum_{i=19}^{22} (\mathrm{C}_i \dot{\ell} + \mathrm{K}_i \ell_i) + \sum_{i=27}^{30} (\mathrm{C}_i \dot{\ell} + \mathrm{K}_i \ell_i) = 0. \end{aligned} \tag{29}$$

Proposition 4 (***Tibia*** **dynamic model.**) *The dynamic model for the Tibia*

$$\begin{aligned} m_4(\ddot{\ell}_{23} + \ddot{\ell}_{24}) - m_1 \sum_{i=15,17} (\ddot{\ell}_i + \ddot{\ell}_{i+1}) + \\ \sum_{i=23}^{24} (\mathrm{C}_i \dot{\ell}_i + \mathrm{K}_i \ell_i) - \sum_{i=15}^{18} (\mathrm{C}_i \dot{\ell}_i + \mathrm{K}_i \ell_i) = 0 \end{aligned} \tag{30}$$

Proposition 5 (***Tarso*** **dynamic model.**) *and the dynamic model for the Tarso muscles network*

$$\begin{aligned} -m_1(\ddot{\ell}_{13} + \ddot{\ell}_{14}) - m_2 \sum_{i=25,27} (\ddot{\ell}_i + \ddot{\ell}_{i+1}) - \\ m_3(\ddot{\ell}_{23} + \ddot{\ell}_{24}) - \sum_{i=13}^{14} (\mathrm{C}_i \dot{\ell}_i + \mathrm{K}_i \ell_i) - \\ \sum_{i=23}^{30} (\mathrm{C}_i \dot{\ell}_i + \mathrm{K}_i \ell_i) = 0 \end{aligned} \tag{31}$$

The next Definition 3 establishes the unit vectors that provide orientations to the *coxa*-limb's muscles. Vector ζ_i has three angles in the form of cosine directions based on the forces of Theorem 1. Calculated cosine directions are shown in Table 6 of Appendix D.

Definition 3 (vector angles) The muscles' director angles according to the muscles shown in Figs. 5 and 6 are defined as

$$\begin{aligned}
\zeta_1 &= (lev.tr.co_\alpha, lev.tr.co_\beta, lev.tr.co_\gamma)^\top\\
\zeta_2 &= (dep.tr_\alpha, dep.tr_\beta, dep.tr_\gamma)^\top\\
\zeta_3 &= (co.fe_\alpha, co.fe_\beta, co.fe_\gamma)^\top\\
\zeta_4 &= (fl.un.tr_\alpha, fl.un.tr_\beta, fl.un.tr_\gamma)^\top\\
\zeta_5 &= (lev.tr.a_\alpha, lev.tr.a_\beta, lev.tr.a_\gamma)^\top\\
\zeta_6 &= (lev.tr.b_\alpha, lev.tr.b_\beta, lev.tr.b_\gamma)^\top\\
\zeta_7 &= (fl.un.p.fe_\alpha, fl.un.p.fe_\beta, fl.un.p.fe_\gamma)^\top\\
\zeta_8 &= (ret.ti.l_\alpha, ret.ti.l_\beta, ret.ti.l_\gamma)^\top\\
\zeta_9 &= (fl.ti_\alpha, fl.ti_\beta, fl.ti_\gamma)^\top\\
\zeta_{10} &= (dep.fe_\alpha, dep.fe_\beta, dep.fe_\gamma)^\top\\
\zeta_{11} &= (pr.fe_\alpha, pr.fe_\beta, pr.fe_\gamma)^\top\\
\zeta_{12} &= (fl.un.fe_\alpha, fl.un.fe_\beta, fl.un.fe_\gamma)^\top\\
\zeta_{13} &= (fl.ta_\alpha, fl.ta_\beta, fl.ta_\gamma)^\top\\
\zeta_{14} &= (pr.ta_\alpha, pr.ta_\beta, pr.ta_\gamma)^\top\\
\zeta_{15} &= (pr.ta.l_\alpha, pr.ta.l_\beta, pr.ta.l_\gamma)^\top
\end{aligned}$$

Theorem 1 (limbs force model) *Each Cartesian component differs in their muscles angular moment, the Newton's second-order law of motion models the sum of components to describe the forces with directions α, β and γ. Thus, Propositions 1-4 are generalized by*

$$\sum_{k=0}^{N}(m_f - m_s)\begin{pmatrix}\ddot{\ell}_x\\ \ddot{\ell}_y\\ \ddot{\ell}_z\end{pmatrix}\cos(\boldsymbol{\zeta}_k) = m\cdot\mathbf{a}, \tag{32}$$

where m_f and m_s are the connected equivalent masses of a muscle at its respective begin and end extremes of each the total N elements.

The inner limb's muscles elastic network is modeled in terms of mass and acceleration for position $\boldsymbol{\Lambda}_{i,j} = (\ddot{\ell}_{x_{i,j}}, \ddot{\ell}_{y_{i,j}}, \ddot{\ell}_{z_{i,j}})^\top$ and $\boldsymbol{\zeta}$ according to Definition 3, by

$$\begin{aligned}
&(m_1 - m_0)[\Lambda_{5,6}\cos(\zeta_1) + \Lambda_{7,8}\cos(\zeta_2)]+\\
&(m_2 - m_0)[\Lambda_{9,10}\cos(\zeta_3) + \Lambda_{11,12}\cos(\zeta_4)]+\\
&m_0[\Lambda_{1,2}\cos(\zeta_5) + \Lambda_{3,4}\cos(\zeta_6)]+\\
&(m_4 - m_1)\Lambda_{13,14}\cos(\zeta_7)+\\
&(m_3 - m_4)\Lambda_{15,16}\cos(\zeta_8)+\\
&(m_3 - m_1)\Lambda_{17,18}\cos(\zeta_9)+\\
&(m_2 - m_1)[\Lambda_{19,20}\cos(\zeta_{10}) + \Lambda_{21,22}\cos(\zeta_{11})]+\\
&(m_4 - m_2)[\Lambda_{27,28}\cos(\zeta_{12}) + \Lambda_{29,30}\cos(\zeta_{13})+\\
&\Lambda_{23,24}\cos(\zeta_{14}) + \Lambda_{25,26}\cos(\zeta_{15})]+\\
&\mathrm{C}_{1,2}\dot{x}_{1,2}\cos(\zeta_5) + \mathrm{C}_{3,4}\dot{x}_{3,4}\cos(\zeta_6) = m\cdot\mathbf{a}.
\end{aligned} \tag{33}$$

where $\mathbf{a} = (\ddot{x}, \ddot{y}, \ddot{z})^{\mathrm{T}}$.

5 Biomechanical control model

In this section, a reduced dynamic network of muscles that is equivalent to the limb's computational model is proposed. This approach facilitates inverse dynamic solutions to predict either lengths of *lev.tr.a* and *lev.tr.b*, or their restitution forces. In addition, a model-based recursive controller is deduced to control the limb's motion. The controller recursively calculates inverse kinematics and use it to estimate forward dynamics and inversely. In model-based control, availability of mathematical models describing the physical system may provide a variety of solution implementations. In this work, the forward model estimates the lengths of $\ell_{1,2}$ by stating the limb's tip desired Cartesian position, $\mathbf{p}^{ref}$. The backward model estimates the input muscles' force $\mathbf{f}_{1,2}$ by knowing the limb's motion speed $\dot{\mathbf{p}}^{ref}$.

Figure 7a-I depicts a similar diagram to Fig. 6ab. Thick lines are parallel/serial muscle connections. For instance, muscles $\ell_{b_{1,2}} \equiv \ell_b$, $\ell_{c_{1,2}} \equiv \ell_c$, $\ell_{e_{1,2}} \equiv \ell_e$, $\ell_{f_{1,2}} \equiv \ell_f$ and $\ell_{h_{1,2,3}} \equiv \ell_h$, such equivalences are formulated by Eq. 54 in Appendix F. From Fig. 7a-I, a simpler equivalent network is shown in Fig. 7a-II, with formulations in Eq. 55. Further simplifications are followed in Figs. 7a-III and 7a-IV, with expressions Eqs. 56 and 57, respectively. A fork-like simplified network model is obtained in this approach to formulate the inverse dynamics.

The three-muscle fork-like network model of Fig. 7b is modeled in terms of muscles' elongation by expression Eq. 34 and deduced in Appendix F, thus

$$\ell_\xi = \ell_{\epsilon_1} + \frac{\ell_{\epsilon_2} + \ell_{deg}}{2} + \frac{\ell_{\epsilon_3} + \ell_h}{2}. \tag{34}$$

Next, let us deduce a dynamic model to obtain posture of the limb's tip (x_ξ, y_ξ, θ_x) using the reduced equivalent network. Let the posture be described as functions of ℓ_1, ℓ_2 and ℓ_ξ.

Let us assume ℓ_2 (*lev.tr.b*) and ℓ_ξ to be collinearly oriented w.r.t. θ_ξ, with Cartesian projection along the x and y axis by

$$x_\xi = (\ell_2 + \ell_\xi)\cos(\theta_\xi) \tag{35a}$$

and

$$y_\xi = (\ell_2 + \ell_\xi)\sin(\theta_\xi). \tag{35b}$$

Thus, bifurcation point at *coxa* (M0), where ℓ_ξ joints with ℓ_1 and ℓ_2 together is $\ell_1 = d_s + \ell_2\cos(\theta_\xi)$, and

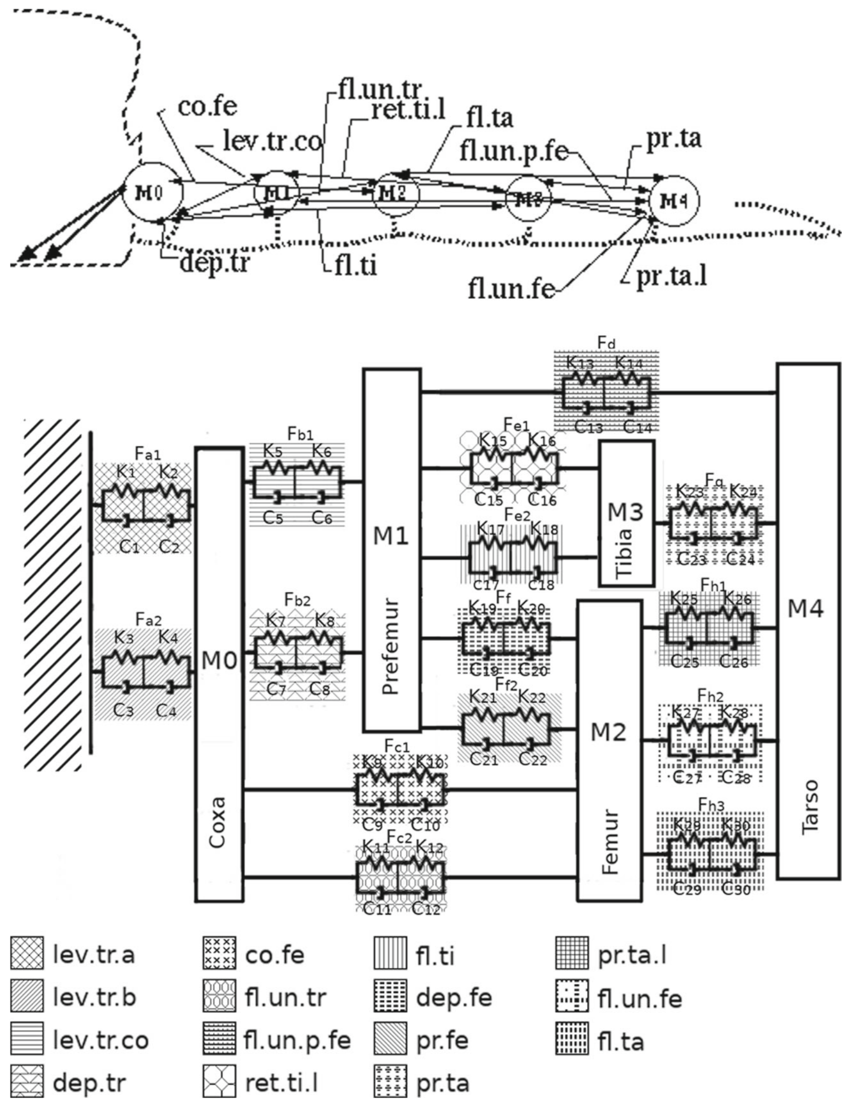

Fig. 6 Limb's muscles system approached by overdamped elastic systems

assuming constant height h. Therefore, the functional form for $\theta_\xi(\ell_1, \ell_2)$ as a function of ℓ_1 and ℓ_2 is

$$\ell_1 - d_s = \ell_2 \cos(\theta_\xi), \tag{36a}$$

dropping off $\cos(\theta_\xi)$,

$$\cos(\theta_\xi) = \frac{\ell_1 - d_s}{\ell_2}, \tag{36b}$$

hence, θ_ξ as a function of ℓ_1 and ℓ_2

$$\theta_\xi = \cos^{-1}\left(\frac{\ell_1 - d_s}{\ell_2}\right). \tag{36c}$$

By substituting previous expression, x_ξ and y_ξ can explicitly be stated in terms of ℓ_1 and ℓ_2,

$$x_\xi = (\ell_2 + \ell_\xi)\cos\left(\cos^{-1}\left(\frac{\ell_1 - d_s}{\ell_2}\right)\right) \tag{37a}$$

and

$$y_\xi = (\ell_2 + \ell_\xi)\sin\left(\cos^{-1}\left(\frac{\ell_1 - d_s}{\ell_2}\right)\right). \tag{37b}$$

Definition 4 ***(Three-muscle equivalent network)*** The equivalent muscles network is defined as ℓ_2 and ℓ_ξ always collinear and ℓ_1 elongates horizontally, with h constant. Therefore, ℓ_1 yields a tangential force that yield angular moment around A by ℓ_2 and ℓ_ξ. The first-order forward solution is

$$\dot{\theta}_\xi = \frac{\dot{\ell}_1 \ell_2}{l_2^2 \sqrt[2]{1 - \left(\frac{\ell_1 - d_s}{\ell_2}\right)}}, \tag{38a}$$

with limb position:

$$\dot{x}_\xi = \dot{\ell}_1\left(1 + \frac{\ell_1 - d_s}{\ell_2} + \ell_1\left(1 + \frac{\dot{\ell}_1 - d_s}{\ell_2}\right)\right) \tag{38b}$$

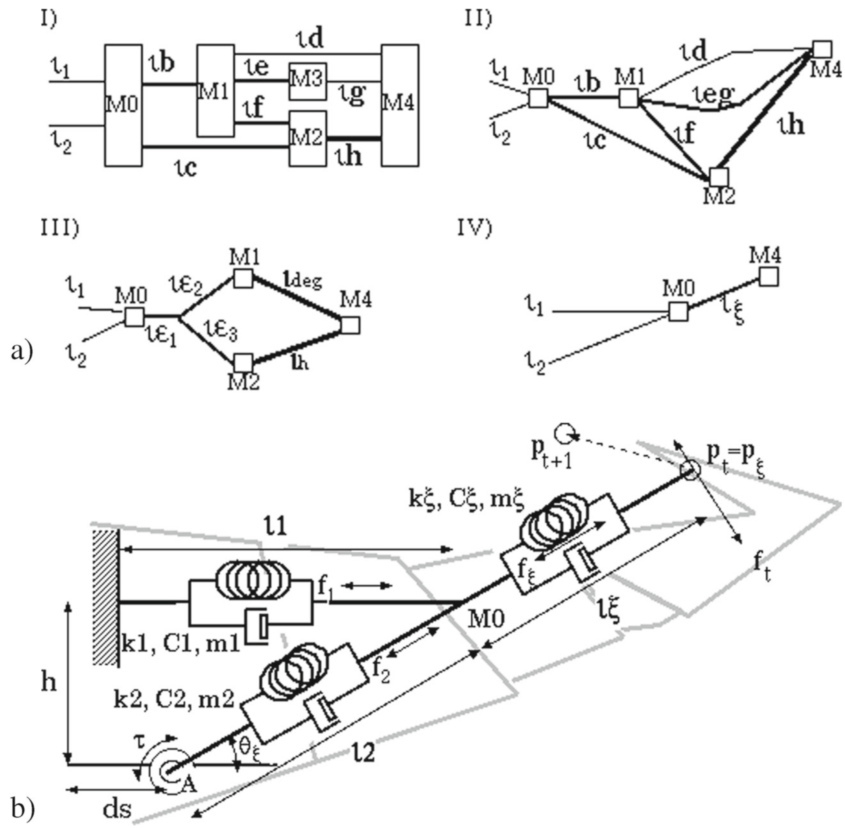

Fig. 7 Equivalent endoskeletal network. **a** parallel muscles $\ell_{b,c,d,f,h}$ (I); serial $\ell_{e,g}$ and Delta net $\ell_{b,c,f}$ (II); serial $\ell_{d,eg}$ and Star net $\ell_{\epsilon1,\epsilon2,\epsilon3}$ (III); serial $\ell_{\epsilon1,deg}$ in parallel with $\ell_{\epsilon3,h}$ (IV). **b** Equivalent net ℓ_ξ and two-input $\ell_{1,2}$

and

$$\dot{y}_\xi = (\dot{\ell}_2 + \dot{\ell}_\xi)\sin\left(\cos^{-1}\left(\frac{\ell_1 - d_s}{\ell_2}\right)\right)\cos^{-1}\left(\frac{\dot{\ell}_1 - d_s}{\ell_2}\right). \tag{38c}$$

From Definition 4, a set of nonlinear equations x_ξ, y_ξ and θ_ξ exists, hence the inverse solution is non trivial and is solved numerically. Thus, starting from the multidimensional Taylor series:

$$x_\xi + \frac{\partial x_\xi}{\partial \ell_1}(\ell_{1_{t+1}} - \ell_{1_t}) + \frac{\partial x_\xi}{\partial \ell_2}(\ell_{2_{t+1}} - \ell_{2_t}) + \frac{\partial x_\xi}{\partial \ell_\xi}(\ell_{\xi_{t+1}} - \ell_{\xi_t}) = 0 \tag{39a}$$

$$y_\xi + \frac{\partial y_\xi}{\partial \ell_1}(\ell_{1_{t+1}} - \ell_{1_t}) + \frac{\partial y_\xi}{\partial \ell_2}(\ell_{2_{t+1}} - \ell_{2_t}) + \frac{\partial y_\xi}{\partial \ell_\xi}(\ell_{\xi_{t+1}} - \ell_{\xi_t}) = 0 \tag{39b}$$

$$\theta_\xi + \frac{\partial \theta_\xi}{\partial \ell_1}(\ell_{1_{t+1}} - \ell_{1_t}) + \frac{\partial \theta_\xi}{\partial \ell_2}(\ell_{2_{t+1}} - \ell_{2_t}) + \frac{\partial \theta_\xi}{\partial \ell_\xi}(\ell_{\xi_{t+1}} - \ell_{\xi_t}) = 0 \tag{39c}$$

By placing the unknown variables of interest at one side of the equality, and the rest of factors at the other side:

$$-x_\xi + \frac{\partial x_\xi}{\partial \ell_1}\ell_{1_t} + \frac{\partial x_\xi}{\partial \ell_2}\ell_{2_t} + \frac{\partial x_\xi}{\partial \ell_\xi}\ell_{\xi_t} = \frac{\partial x_\xi}{\partial \ell_1}\ell_{1_{t+1}} + \frac{\partial x_\xi}{\partial \ell_2}\ell_{2_{t+1}} + \frac{\partial x_\xi}{\partial \ell_\xi}\ell_{\xi_{t+1}}, \tag{40a}$$

as well as

$$-y_\xi + \frac{\partial y_\xi}{\partial \ell_1}\ell_{1_t} + \frac{\partial y_\xi}{\partial \ell_2}\ell_{2_t} + \frac{\partial y_\xi}{\partial \ell_3}\ell_{3_t} = \frac{\partial y_\xi}{\partial \ell_1}\ell_{1_{t+1}} + \frac{\partial y_\xi}{\partial \ell_2}\ell_{2_{t+1}} + \frac{\partial y_\xi}{\partial \ell_\xi}\ell_{\xi_{t+1}} \tag{40b}$$

and

$$-\theta_\xi + \frac{\partial \theta_\xi}{\partial \ell_1}\ell_{1_t} + \frac{\partial \theta_\xi}{\partial \ell_2}\ell_{2_t} + \frac{\partial \theta_\xi}{\partial \ell_\xi}\ell_{\xi_t} = \frac{\partial \theta_\xi}{\partial \ell_1}\ell_{1_{t+1}} + \frac{\partial \theta_\xi}{\partial \ell_2}\ell_{2_{t+1}} + \frac{\partial \theta_\xi}{\partial \ell_\xi}\ell_{\xi_{t+1}}. \tag{40c}$$

Redefining the temporal terms A_1, A_2 and A_3 as,

$$A_1 = -x_\xi + \frac{\partial x_\xi}{\partial \ell_1}\ell_{1_t} + \frac{\partial x_\xi}{\partial \ell_2}\ell_{2_t} + \frac{\partial x_\xi}{\partial \ell_3}\ell_{3_t}, \tag{41a}$$

$$A_2 = -y_\xi + \frac{\partial y_\xi}{\partial \ell_1}\ell_{1_t} + \frac{\partial y_\xi}{\partial \ell_2}\ell_{2_t} + \frac{\partial y_\xi}{\partial \ell_3}\ell_{3_t}, \tag{41b}$$

and

$$A_3 = -\theta_\xi + \frac{\partial \theta_\xi}{\partial \ell_1}\ell_{1_t} + \frac{\partial \theta_\xi}{\partial \ell_2}\ell_{2_t} + \frac{\partial \theta_\xi}{\partial \ell_3}\ell_{3_t}. \tag{41c}$$

Thus, from Eq. 40 the set of linear equations is

$$A_1 = \frac{\partial x_\xi}{\partial \ell_1}\ell_{1_{t+1}} + \frac{\partial x_\xi}{\partial \ell_2}\ell_{2_{t+1}} + \frac{\partial x_\xi}{\partial \ell_\xi}\ell_{\xi_{t+1}}, \tag{42a}$$

as well as

$$A_2 = \frac{\partial y_\xi}{\partial \ell_1}\ell_{1_{t+1}} + \frac{\partial y_\xi}{\partial \ell_2}\ell_{2_{t+1}} + \frac{\partial y_\xi}{\partial \ell_\xi}\ell_{\xi_{t+1}} \tag{42b}$$

and

$$A_3 = \frac{\partial \theta_\xi}{\partial \ell_1}\ell_{1_{t+1}} + \frac{\partial \theta_\xi}{\partial \ell_2}\ell_{2_{t+1}} + \frac{\partial \theta_\xi}{\partial \ell_\xi}\ell_{\xi_{t+1}}. \tag{42c}$$

Expressing in the matrix form $\boldsymbol{A} = \mathbf{Q} \cdot \boldsymbol{\Lambda}$, where $\boldsymbol{A} = (A_1, A_2, A_3,)^\top$, $\boldsymbol{\Lambda} = (\ell_{1_{t+1}}, \ell_{2_{t+1}}, \ell_{\xi_{t+1}})^\top$ and $\mathbf{Q}$ is the Jacobian matrix,

$$\begin{pmatrix} A_1 \\ A_2 \\ A_3 \end{pmatrix} = \begin{pmatrix} \frac{\partial x_\xi}{\partial \ell_1} & \frac{\partial x_\xi}{\partial \ell_2} & \frac{\partial x_\xi}{\partial \ell_\xi} \\ \frac{\partial y_\xi}{\partial \ell_1} & \frac{\partial y_\xi}{\partial \ell_2} & \frac{\partial y_\xi}{\partial \ell_\xi} \\ \frac{\partial \theta_\xi}{\partial \ell_1} & \frac{\partial \theta_\xi}{\partial \ell_2} & \frac{\partial \theta_\xi}{\partial \ell_\xi} \end{pmatrix} \cdot \begin{pmatrix} \ell_{1_{t+1}} \\ \ell_{2_{t+1}} \\ \ell_{\xi_{t+1}} \end{pmatrix} \tag{43}$$

where the Jacobian matrix elements are defined by:

$$\frac{\partial x_\xi}{\partial \ell_1} = \frac{\ell_2 + \ell_\xi}{\ell_2}, \quad \frac{\partial x_\xi}{\partial \ell_2} = \frac{\ell_1 - d_s}{\ell_2}\left[1 - \frac{(\ell_2 - \ell_\xi)}{\ell_2}\right],$$

$$\frac{\partial x_\xi}{\partial \ell_\xi} = \frac{\ell_1 - d_s}{\ell_2}$$

and

$$\frac{\partial y_\xi}{\partial \ell_1} = -\frac{(\ell_2 - \ell_\xi)(\ell_1 - d_s)}{\ell_2^2 \sqrt[2]{1 - \left(\frac{\ell_1 - d_s}{\ell_2}\right)^2}}, \quad \frac{\partial y_\xi}{\partial \ell_2} = \frac{(\ell_1 + \ell_3)(\ell_2 - d_s)}{\ell_1^3 \sqrt[2]{1 - \left(\frac{\ell_2 - d_s}{\ell_1}\right)^2}},$$

$$\frac{\partial y_\xi}{\partial \ell_\xi} = \sqrt[2]{1 - \left(\frac{\ell_1 - d_s}{\ell_2}\right)^2},$$

$$\frac{\partial \theta_\xi}{\partial \ell_1} = -\frac{1}{\ell_2 \sqrt[2]{1 - \left(\frac{\ell_1 - d_s}{\ell_2}\right)^2}},$$

and finally,

$$\frac{\partial \theta_\xi}{\partial \ell_2} = \frac{\ell_1 - d_s}{\ell_2^2 \sqrt[2]{1 - \left(\frac{\ell_1 - d_s}{\ell_2}\right)^2}}, \quad \frac{\partial \theta_\xi}{\partial \ell_\xi} = 0.$$

Therefore, a linearized inverse recursive solution is

$$\boldsymbol{\Lambda}_{t+1} = \boldsymbol{\Lambda}_t + \mathbf{Q}_t^{-1} \cdot \boldsymbol{A}_t \tag{44}$$

the recursion is stopped until the convergence criterion $\left|\frac{\boldsymbol{\Lambda}_{t+1} - \boldsymbol{\Lambda}_t}{\boldsymbol{\Lambda}_{t+1}}\right| < \epsilon_\lambda$ is established true,

5.1 ℓ_1, ℓ_2 length control by limb's position $\Lambda(\mathrm{p}^{ref})$

The inverse kinematics is obtained from Eq. 3, where $\mathbf{p}^{ref}$ is a desired limb position. Joints are inferred recursively,

$$\boldsymbol{\Phi}_{t+1} = \boldsymbol{\Phi}_t + \mathbf{J}_t^+ \cdot (\mathbf{p}^{\mathbf{ref}} - \hat{\mathbf{p}}_\mathbf{t}), \tag{45a}$$

then, $\boldsymbol{\Phi}^{ref} = \boldsymbol{\Phi}_{t+1}$ will predict the limb position:

$$\mathbf{p}_{t+1} = \mathbf{p}_t + \mathbf{J}_t \cdot (\boldsymbol{\Phi}^{\mathbf{ref}} - \hat{\boldsymbol{\Phi}}_\mathbf{t}) \tag{45b}$$

and matrices $\mathbf{J}_t = \mathbf{J}_{t+1}(\boldsymbol{\Phi}_{t+1})$ and $\mathbf{J}_t^+ = \mathbf{J}_{t+1}^+$ are updated. The recursive process finishes until the relative error rate converges less than $\epsilon_\mathbf{p}$

$$\left\|\frac{\mathbf{p}^{ref} - \mathbf{p}_t}{\mathbf{p}^{ref}}\right\| < \epsilon_\mathbf{p}. \tag{45c}$$

Hence, the limb $\mathbf{p}_{t+1}$ is obtained by forward kinematics, being equivalent to model Eq. 37, such that

$$\mathbf{p}_\epsilon \equiv \mathbf{p}_{t+1}, \quad \theta_\epsilon = \arctan\left(\frac{y_{t+1}}{x_{t+1}}\right) \tag{45d}$$

and the controller recursively infers ℓ_1 and ℓ_2,

$$\boldsymbol{\Lambda}_{t+1} = \boldsymbol{\Lambda}_t + \mathbf{Q}_t^{-1} \cdot \mathbf{A}_t \tag{45e}$$

until convergence is reached with numeric precision ϵ_λ,

$$\left\|\frac{\boldsymbol{\Lambda}_{t+1} - \boldsymbol{\Lambda}_t}{\boldsymbol{\Lambda}_{t+1}}\right\| < \epsilon_\lambda \tag{45f}$$

Therefore, lengths ℓ_1 and ℓ_2 are initially obtained from estimating $\boldsymbol{\Phi}_{t+1}$.

5.2 Control of $\mathrm{f}_{1,2}$ by limb's speed $\mathrm{f}_{1,2}(\dot{\mathrm{p}}^{ref})$

Restitution forces for ℓ_1 (*lev.tr.a*) and ℓ_2 (*lev.tr.b*) are controlled in terms of limb's speed $\dot{\mathbf{p}}^{ref}$, initially stated in Eq. 3 and recursively inferred by,

$$\boldsymbol{\Phi}_{t+1} = \boldsymbol{\Phi}_t + \mathbf{J}_t^+ \cdot (\mathbf{p}^{ref} - \hat{\mathbf{p}}_t), \tag{46a}$$

the limb's position prediction by the forward model is

$$\mathbf{p}_{t+1} = \mathbf{p}_t + \mathbf{J}_t \cdot (\boldsymbol{\Phi}^{\mathbf{ref}} - \hat{\boldsymbol{\Phi}}_\mathbf{t}), \tag{46b}$$

where

$$\triangle\mathbf{J}_t = \mathbf{J}_{t+1} - \mathbf{J}_t; \quad \triangle\boldsymbol{\Phi}_t = \boldsymbol{\Phi}_{t+1} - \boldsymbol{\Phi}_t \tag{46c}$$

using previous terms, the first-order expressions are

$$\dot{\mathbf{p}}_{t+1} = \dot{\mathbf{p}}_t + \triangle\mathbf{J} \cdot \triangle\boldsymbol{\Phi}_t + \mathbf{J}_t \cdot (\dot{\boldsymbol{\Phi}}^{\mathbf{ref}} - \hat{\dot{\boldsymbol{\Phi}}}_\mathbf{t}), \tag{46d}$$

where $\mathbf{p}^{ref} \equiv \mathbf{p}_{t+1}$, then

$$\dot{\boldsymbol{\Phi}}_{t+1} = \dot{\boldsymbol{\Phi}}_t + \mathbf{J}_t^+(\dot{\mathbf{p}}^{ref} - \hat{\dot{\mathbf{p}}}_t - \triangle\mathbf{J}_t \cdot \triangle\boldsymbol{\Phi}_t). \tag{46e}$$

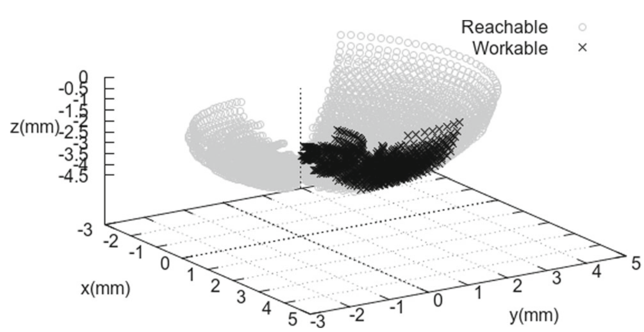

Fig. 8 Compliant (reachable) and workable (controlled) space by using *lev.tr.a* (ℓ_1) and *lev.tr.b* (ℓ_2)

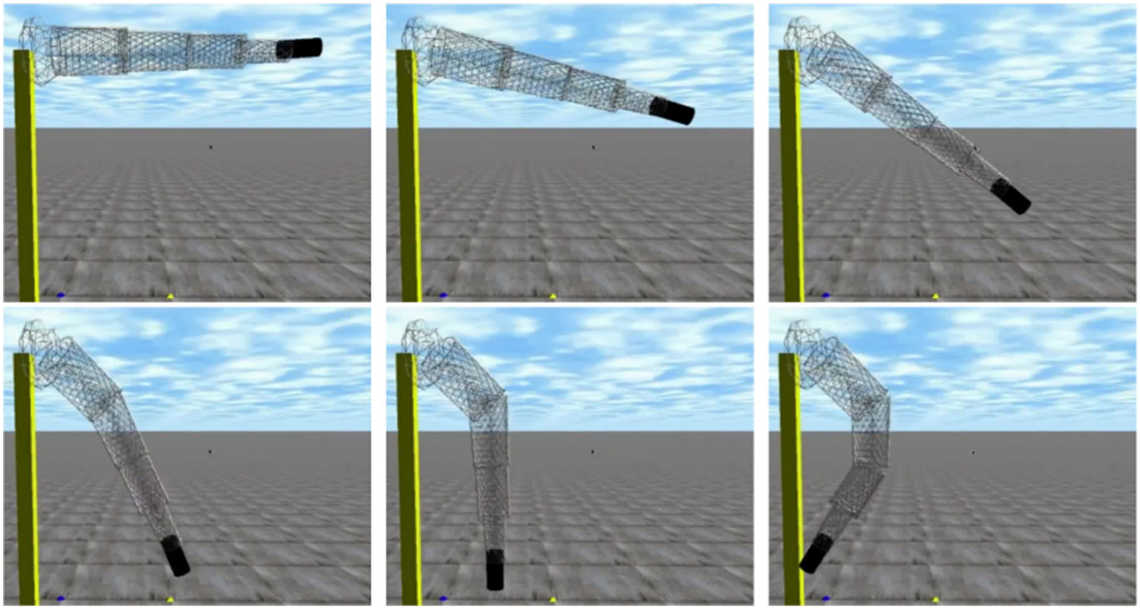

Fig. 9 ODE-based 3D wireframe limb, arbitrary motions of *lev.tr.a* are predominant over *lev.tr.b*

Therefore, $\mathbf{p}_{t+1}$ and $\dot{\mathbf{p}}_{t+1}$ are used next to determine muscles elongations and speeds by

$$\boldsymbol{\Lambda}_{t+1} = \boldsymbol{\Lambda}_t + \mathbf{Q}^{-1} \cdot \mathbf{A}(\mathbf{p}_{t+1}), \tag{46f}$$

then with prediction and actual values a general approach is

$$\dot{\boldsymbol{\Lambda}} = \frac{\mathrm{d}}{\mathrm{d}t}\boldsymbol{\Lambda} = \frac{\Lambda_{t+1} - \Lambda_t}{t_2 - t_1},$$

and substituting next

$$\dot{\boldsymbol{\Lambda}}_{t+1} = \dot{\boldsymbol{\Lambda}}_t + \dot{\mathbf{Q}}^{-1} \cdot \mathbf{A}(\mathbf{p}_{t+1}) + \mathbf{Q}^{-1} \cdot \dot{\mathbf{A}}(\dot{\mathbf{p}}_{t+1}). \tag{46g}$$

Thus, the instantaneous muscle forces are,

$$\mathbf{f}_t = \begin{pmatrix} f_1 \\ f_2 \\ f_\xi \end{pmatrix} = \begin{pmatrix} m_1 & 0 & 0 \\ 0 & m_2 & 0 \\ 0 & 0 & m_\xi \end{pmatrix} \cdot \frac{\mathrm{d}}{\mathrm{d}t} \begin{pmatrix} \dot{\ell}_1 \\ \dot{\ell}_2 \\ \dot{\ell}_\xi \end{pmatrix}. \tag{46h}$$

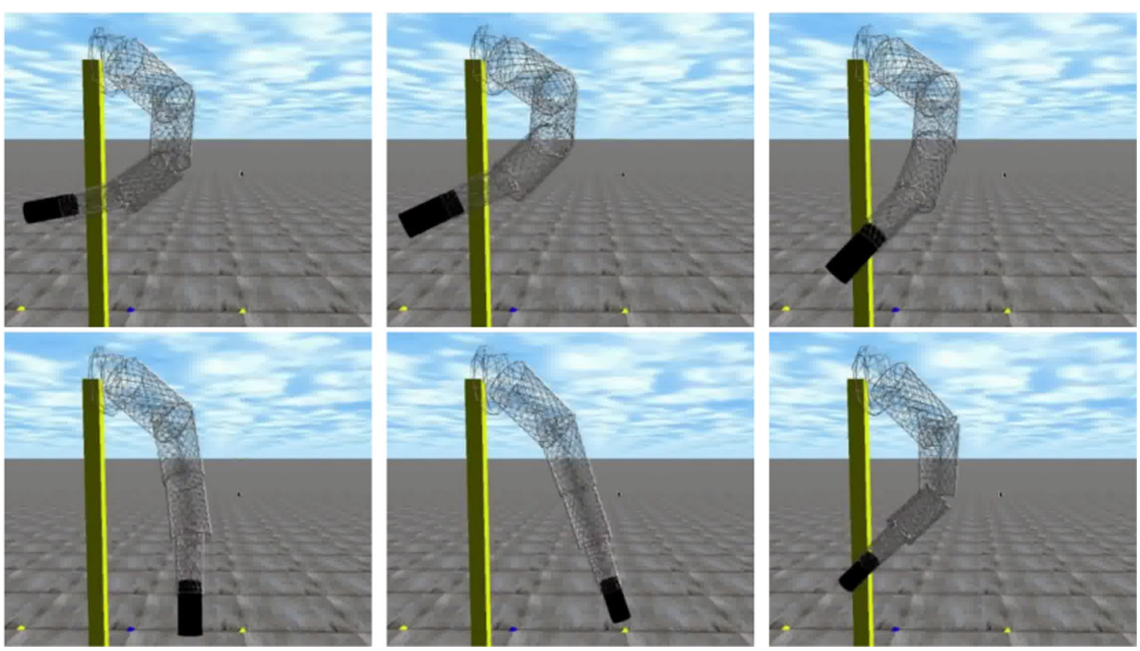

Fig. 10 Motion behavior when *lev.tr.a* and *lev.tr.b* are similar inputs

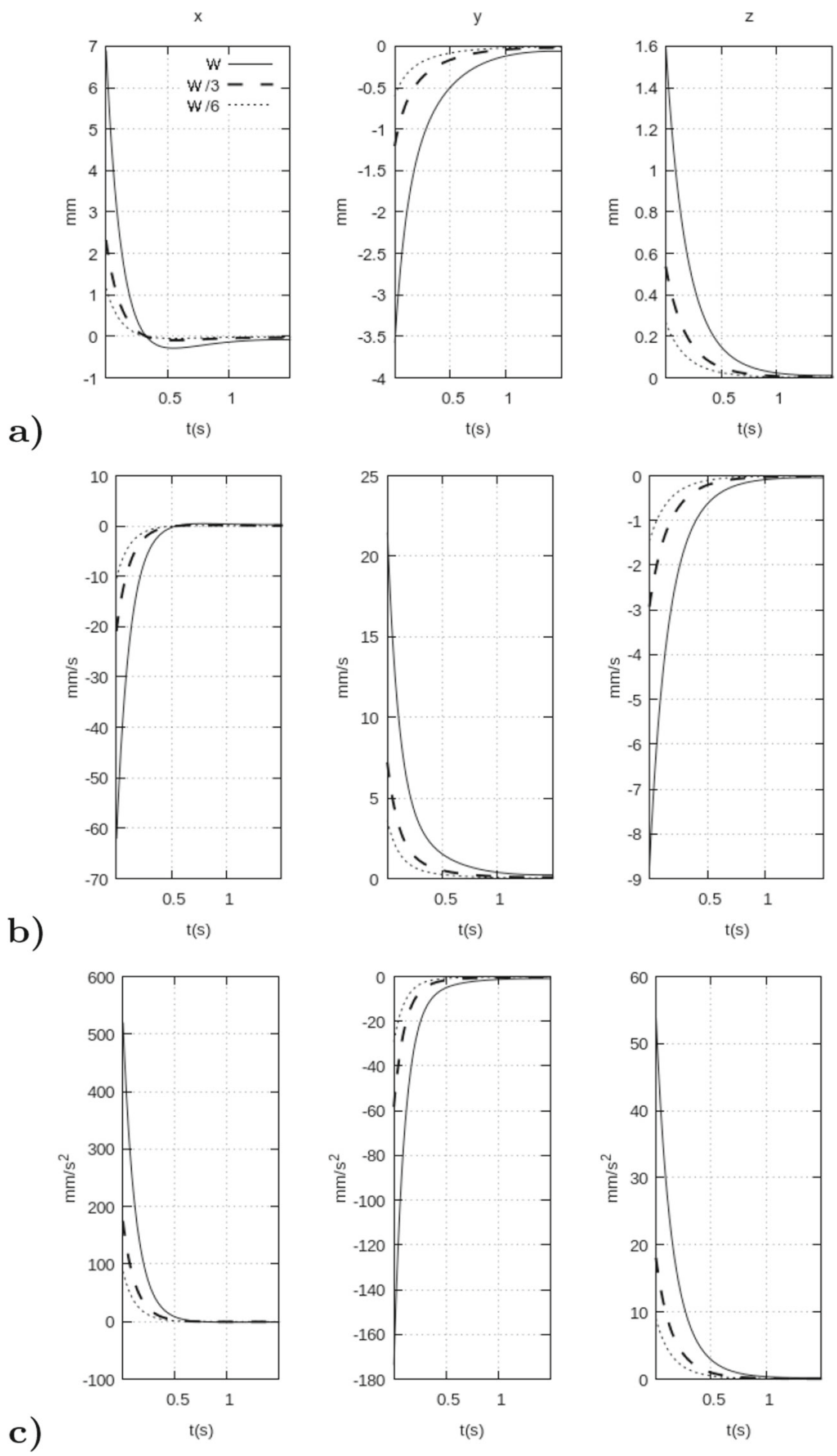

Fig. 11 Limb's motion effects varying $W_{1..4}$. **a)** xyz displacements. **b)** xyz velocities. **c)** xyz accelerations

Moreover, the limb's tip tangential force f_T is of interest, thus the angular moment $M_A = I\ddot{\theta}_\xi$ at the point A, w.r.t. θ_ξ is equivalent to torque τ, such that $M_A = f_T(\ell_1 + \ell_\xi)$, thus

$$M_A = f_T(\ell_1 + \ell_\xi), \tag{47}$$

hence, by dropping off f_T

$$f_T = \frac{I\ddot{\theta}_\xi}{\ell_2 + \ell_\xi}, \tag{48}$$

where $I = r^2 m$ assumes each muscle shape as cylinders. For known values of $\ell_{1,\xi}$ when $\mathbf{p}_{t+1}$ is known a priori,

$$f_T = \frac{I}{\ell_2 + \ell_\xi} = \frac{\mathrm{d}}{\mathrm{d}t}\left(\frac{\dot{\ell}_2}{\dot{\ell}_2^2 \sqrt[2]{1 - \frac{\ell_1 - d_s}{\ell_2}}}\right), \tag{49}$$

Furthermore, the time model to reach a reference position $\dot{\mathbf{p}}^{ref}$, while applying a force,

$$t_2 = t_1 + (af_2)^{-1}(\dot{\mathbf{p}}^{ref} - \hat{\dot{\mathbf{p}}}_t), \tag{50a}$$

where, $\hat{\dot{\mathbf{p}}}_t$ is the actual limb's position tided to reach $\dot{\mathbf{p}}^{ref}$ at time prediction t_2, while projected into future $\dot{\mathbf{p}}_{t+1}$, taken as reference time in next expression:

$$\dot{\mathbf{p}}_{t+1} = \dot{\mathbf{p}}_t + af_2(t_2 - \hat{t}_1). \tag{50b}$$

Additionally to Definition 4, with the time prediction at hand, alternative dynamic muscles' model in particular for *lev.tr.ab* are available:

$$\begin{aligned} \dot{\ell}_1 &= -W_1\lambda_1 \mathrm{e}^{-\lambda_1 t} - W_2\lambda_2 \mathrm{e}^{-\lambda_2 t} \\ \dot{\ell}_2 &= -W_3\lambda_3 \mathrm{e}^{-\lambda_3 t} - W_4\lambda_4 \mathrm{e}^{-\lambda_4 t} \\ \dot{\ell}_\xi &= -W_5\lambda_5 \mathrm{e}^{-\lambda_5 t} - W_6\lambda_6 \mathrm{e}^{-\lambda_6 t} \end{aligned} \tag{51}$$

6 Results and discussion

Although, this work's purpose is not focused on yielding *Chilopoda*'s locomotion or gait patterns [31], the present control approach provides flexibility to meet different limb's motion behaviors throughout a pair of input muscles *lev.tr.a* and *lev.tr.b*. The reference models previously defined (e.g. $\mathbf{p}^{ref}$, $\dot{\mathbf{p}}^{ref}$) are critical because they represent either experimental data or analytic functions about a centipede's gait. These reference models fit to positions and/or higher-order kinematic derivatives arising from linear or nonlinear functions.

Figure 8 shows the limb's motion space, with Cartesian origin in the middle of *coxa* and *prefemur*. The controlled motion (workable space) is eventually produced by using the pair of muscles *lev.tr.a* and *lev.tr.b*.

The proposed dynamic model was implemented in a standard capability computer under a Linux system. The algorithms were coded and compiled in GNU C/C++. Animated simulations included the use of a physics engine library Object Dynamic Engine (ODE). The limb is a wireframe structure constructed by a spherical joint for link l_0, and rotatory joints for $l_{1,\ldots,4}$ (See Figs. 9 and 10).

Fig. 12 ODE simulation torque for equivalent network

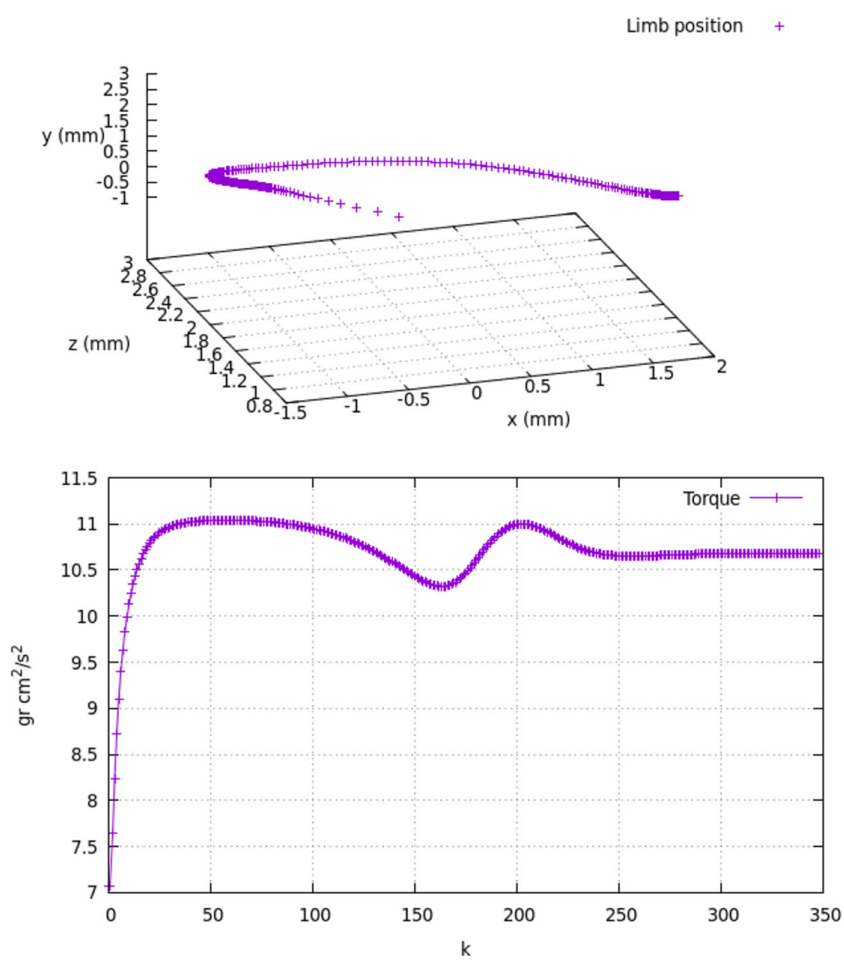

Table 2 Simulation dynamical properties

Kinematic properties			
l_1 (mm)	1.1418	l_3 (mm)	0.8658
l_2 (mm)	1.1115	l_4 (mm)	1.4119
Kinetic properties			
m_0(gr)	2.0	m_3(gr)	1.7
m_1(gr)	2.0	m_4(gr)	1.0
m_2(gr)	2.5	W(mm)	2.0
K_a (gr/s^2)	20	C_{coxa}(gr/s)	26.698
K_b	10	$C_{prefemur}$	26.698
K_c	11	C_{femur}	29.85
K_d	10	C_{tibia}	24.615
K_e	5	C_{tarso}	18.879
K_f	9	K_g	9.0
K_h	9	Δt (s)	0.01

Figure 9 shows six simulation video frames illustrating the limb's controlled motion for arbitrary trajectories. In this simulation the motions magnitudes of the muscle *lev.tr.a* are more predominant than the elongations of *lev.tr.b* (Fig. 11).

Figure 10 depicts six video frames that resume simulations on the trajectories yielded when *lev.tr.b* is more or less similar to the motions of *lev.tr.a*. Figure 12 shows some equivalent dynamic properties.

Figure 11a depicts Cartesian elongation/contraction motion of the whole network of muscles. According to the dynamic parameters, the system is experiencing either critically damped or overdamped effects, which is an advantage because shows dissipation capability when vibrations are produced by external noise. In these simulations, the metric amplitude for each muscle W includes alternative values, above and below the average value. Although, while in the metric displacement, the x and the yz components yield critically and overdamped effects respectively, in Fig. 11bc both linear velocities and accelerations exhibit an overdamped stability behavior.

Table 2 shows some dynamic properties used to obtain the results depicted in Figs. 9, 10 and 11. The proposed approach does not explcity models the mechanical energies

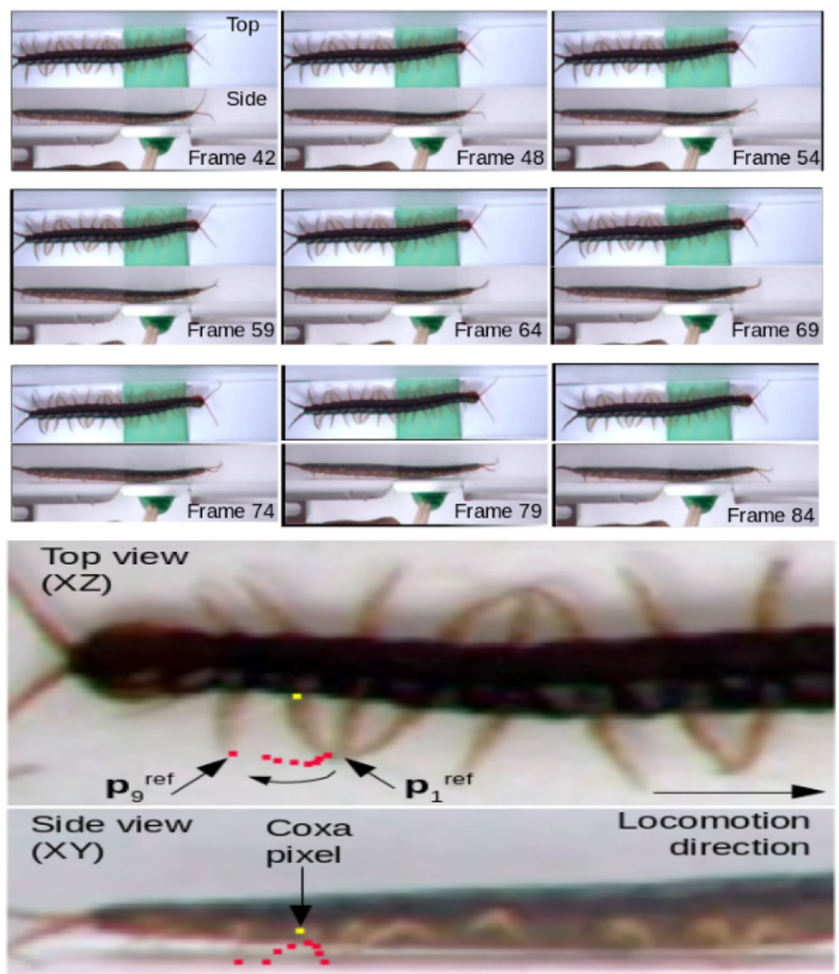

Fig. 13 Centipede's gait pixels tracking. The *coxa*'s pixel was used as local Cartesian reference coordinate. Video frames provided by [19] in publisher's site

of the system as it does not follow an energy-based Euler-Lagrange approach, but follows a Newton-Euler-based solution. Table 2 not necessarily represent the exact biological Centipede's parameters, some data were adjusted by the authors in order to improve numerical visualization during simulates animations (most other dynamical parameters that could be set fixed were calculated online). This work's purpose differs from other similar researches, where our primary objective is to model the limb's inner network of muscles and see its underactuated effects by two input muscles, instead of generating gaiting patterns and/or Chilopoda locomotion behaviors. Such as the case of [32] where a *Chilopoda* of same taxonomic order, the *Scolopendromorpha*[2] is studied in terms of its gait locomotion wave patterns to change direction. Likewise, the work [33] reported an study on amphibious adaptation during transition between terrestrial and aquatic environments for a centipede *Scolopendra subspinipes mutilans*.

Nevertheless, in order to validate and show effectiveness of the proposed model, we collected the experimental videos 1 and 2 that were provided Yasui K. et al. (Fig. 13). We found these experimental data suitable enough to validate our approach.

In such a reference, a *Chilopoda* motion is video recorded by two cameras (same optical features) placed at top and side locations. Although video cameras do not provide metric data about the Centipede's limbs, authors of the present research processed individual frames that compounded the videos in order to calculate one limb's gait cycle. The main purpose of this digital image process was to extract a set of Cartesian points tracked by the Chilopoda's limb to be treated as the reference trajectory. Due to image resolution and low sharpness quality (in particular the side view frames) only nine points were tracked with the less noise possible to complete a gait cycle. The gait's points represent nine reference 3D positions $\mathbf{p}_k^{ref}$ for $k = 1, 2, \ldots, 9$.

The camera calibration is the process of recovering metric information from the image planes. In this work, the calibration model is basically as same as the reference points $\mathbf{p}_k^{ref}$. The following cameras model was used to infer the Cartesian measurements of one limb's positions. Thus, by using the top and side views, the orientation angle φ_{xz} of the limb's tip w.r.t. the coxa at the xz plane is

$$\varphi_{xz} = \arctan\left(\frac{\Delta\rho_C}{\Delta\rho_R}\right), \tag{52}$$

the pixels distance between coxa's coordinate (ρ_C^c, ρ_R^c) and limb's tip coordinate (ρ_C, ρ_R) are

$$\Delta\rho_C = \rho_C^c - \rho_C, \quad \Delta\rho_R = \rho_R^c - \rho_R.$$

The nominal image resolution [mm/pixel] for columns ratio f_x and rows ratio f_y, assuming that both cameras (top xz and side xy) are identical, then $f_x^{xz} \equiv f_x^{xy}$ and $f_z^{xz} \equiv f_y^{xy}$. Hence,

$$f_x = \frac{X_{back}}{N_C}, \quad f_z = \frac{Z_{back}}{N_R},$$

where, XYZ_{back} are the background metric lengths scoped by the camera field of view and were inferred by a linear

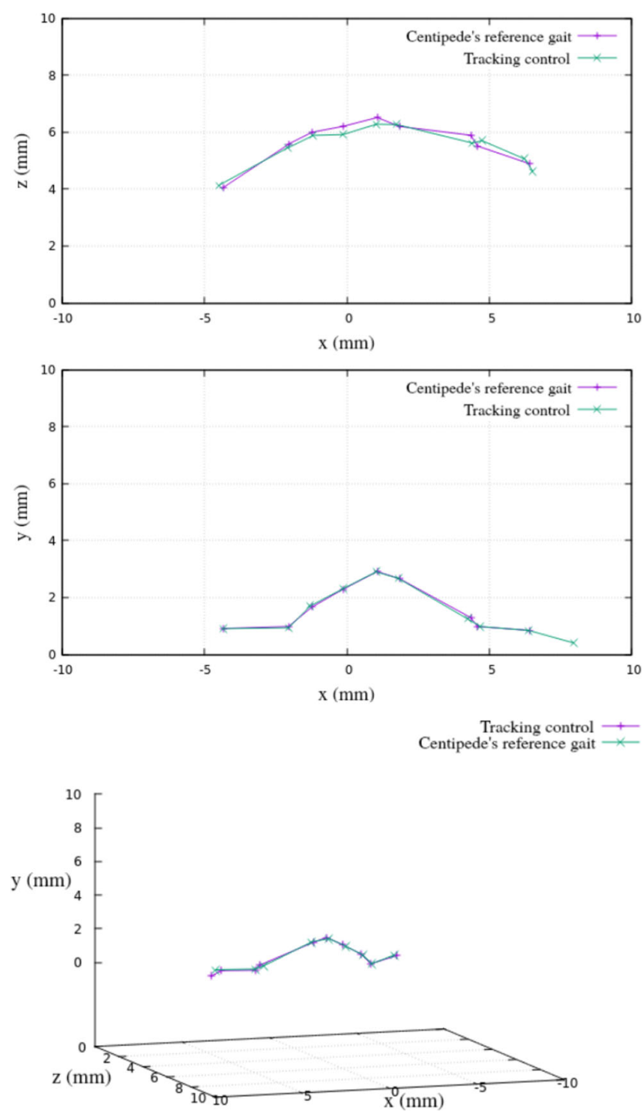

Fig. 14 Centipede's gait tracking control

[2] *Scolopocryptops rubiginosus* L. Koch centipede.

metric relationship known by the real Centipede's metric size. Likewise, $N_R \times N_C$ is the image resolution:

$$\mathbf{p}_k^{ref} = \begin{pmatrix} \sqrt[2]{(\Delta\rho_C \cdot f_x)^2 + (\Delta\rho_R \cdot f_z)^2}\,\sin(\varphi_{xz}) \\ \left|\rho_{xy}^o - \rho_{xy}^R\right| \left(\frac{Y_{back}}{N_R}\right) \\ \sqrt[2]{(\Delta\rho_C \cdot f_x)^2 + (\Delta\rho_R \cdot f_z)^2}\,\cos(\varphi_{xz}) \end{pmatrix}, \quad (53)$$

where the scene's floor vertical pixel reference in the plane xy is ρ^o, and the limb's end is ρ^y. Therefore, at each image frame the limb's tip pixels coordinate is at (ρ_k^C, ρ_k^R). For this experiment, the limb's reference positions denoted by $\mathbf{p}_1^{ref}, \ldots, \mathbf{p}_9^{ref}$ are shown in Fig. 14 as the reference Centipede's gait. The tracking control trajectory follows the reference gait points, and therefore represents the effectiveness of the proposed limb's dynamic trackig control.

7 Conclusion

From different planar taxonomic views reported by biologists in the scientific literature, in this work we have presented the Chilopoda's limb muscular system in 3D, which was built geometrically by means of polygonal matching. We conclude that the musculoskeletal connections were biomechanically consistent with the 3D polygonal matched model because their projections over the taxonomic planes were equivalent. From the disclosed 3D musculoskeletal model, a reduced muscular system was proposed that consistently emulated the equivalent motion of a complete biological *chilopoda*'s limb. The kinematic constraint and laws governing the reduced muscular system motion was coherent compared with bibliographic reported material. The mathematical model describing the simplified limb's musculoskeletal 3D motion was deduced, with good controllability, dexterity and motion resolution. The network of elastic elements (muscles) allowed the analysis and validation about the dynamics of the 3D limb's biomechanics. Having the artificial muscles, the elasticity and dampening coefficients were estimated by manual adjusting, which were equivalents to the *Centipede*'s muscles in millimeters scale. Through the proposed dynamic model was proved that the four joints (*coxa*, *prefemur*, *tibia* and *tarso*) and the inner network of muscles can realistically be controlled by means of only two control input muscles from the *coxa*, *lev.tr.a* and *lev.tr.b*. A set of images frames extracted from real experimental top and side videos on Centipede's locomotion were taken as validation data. The real Centipede limb's gait was metrically calculated to represent the set of reference points $\mathbf{p}_k^{ref}$. Tracking control demonstrated the validity and effectiveness of the proposed model to accurately follow a cycle gait.

Appendix A: Muscles spatial vectors

Table 3 Muscles local Cartesian vectors

Muscle	x	y	z
Vectors *trunk – coxa*			
dvc	0.283823	2.42299	–0
dvc.a	0.53162	0.178111	–0.144076
dvc.1	–0.0537923	–0.51629	0.465783
dvc.2	0.0492127	–0.48288	–0.148438
dvc.3	–0.314205	–0.366093	0.266286
dvc.4	–0.826191	–0.514065	0.0666297
rot.trp	–0.823967	1.20077	–0.80671
pclx	–0.294956	0.591413	–1.27856
tcx	–0.614395	0.705609	–1.21438
tep	–0.341857	0.852939	–0.188288
rot.tr	–0.571187	0.678299	–0.448729
pct.1	–0.0216041	0.815354	1.19871
pct.2	–0.0216041	0.854303	0.97963
ret.cos	–1.92313	2.6278	–1.59876
ret.trt	–0.757779	–0.370891	–0.588648
ret.trs	–2.04362	–0.448584	–0.58574
pr.tr.co.a	–1.75638	2.72539	1.16473
pr.tr.co.b	–2.19002	2.7579	0.478868
pr.cot	–0.586189	–0.166015	1.24596
lev.tr.a	–1.91697	–1.14027	0.396057
lev.tr.b	–1.7406	–1.13435	0.0362734
Vectors *Coxa* – leg's tip			
pr.ta E	0.128956	–0.124584	0.183548
re.ti E	1.10537	–0.228331	0.207842
fl.ta E	1.19067	–0.436205	0.00164285
pr.ta.l E	0.877384	–0.0459183	0.00180277
fl.ti E	2.07231	0.430633	0.175537
fl.un.p.fe E	2.78483	–0.0810722	–0.136167
fl.un.fe E	0.995665	–0.42592	0.0441969
dep.fe E	0.826902	0.129965	–0.0179841
co.fe E	1.55459	0.748069	0.0753528
fl.un.tr E	1.02399	0.292072	0.448555
pr.fe E	0.238628	0.364539	–0.0634313
co.fe	–1.58734	–0.565637	–0.127153
re.ti.l	1.00977	–0.83153	0.265341
fl.ta	0.605271	–1.22357	–0.0438771
pr.ta.l	0.747108	–1.03269	–0
pr.ta	0.0580041	–0.367416	0.157451
pr.fe	–0.288898	–0.207974	0.0567872
fl.ti	1.89324	–0.252076	0.169736
fl.un.p.fe	2.42277	–1.44575	–0.136705
fl.un.tr	0.923576	–0.126688	0.39751
fl.un.fe	0.415119	–1.10395	–0.0193071
lev.tr.co	–0.272448	–0.543866	–0.142375
dep.fe	–0.790407	0.020207	0.049329
dep.tr	0.531036	0.0218455	0.0479478

Appendix B: Muscles length

Table 4 Muscles metric length

Muscle	Length (mm)	Muscle	Length (mm)
dvc	2.43956	re.ti E	1.14768
dvc.a	0.57888	fl.ta E	1.26806
dvc.1	0.697426	pr.ta.l E	0.878587
dvc.2	0.507572	fl.ti E	2.12384
dvc.3	0.551051	fl.un.p.fe E	2.78934
dvc.4	0.975343	fl.un.fe	1.08384
rot.trp	1.6648	dep.fe E	0.837246
pclx	1.43926	co.fe E	1.72686
tcx	1.533	fl.un.tr E	1.15545
tep	0.937989	pr.fe E	0.44029
rot.tr	0.993832	co.fe	1.6899
pct.1	1.44989	re.ti.l	1.33472
pct.2	1.29999	fl.ta	1.3658
ret.cos	3.62765	pr.ta.l	1.2746
ret.trt	1.02873	pr.ta	0.403918
ret.trs	2.17272	pr.fe	0.360472
pr.tr.co.a	3.44518	fl.ti	1.91747
pr.tr.co.b	3.55408	fl.un.p.fe	2.82466
pr.cot	1.38694	fl.un.tr	1.01344
lev.tr.a	2.26536	fl.un.fe	1.17958
lev.tr.b	2.07793	lev.tr.co	0.624731
pr.ta E	0.256595	dep.fe	0.792203
		dep.tr	0.533644

Appendix C: Endoskeleton unit vectors

Table 5 Normalized vectors

Vectors *trunk* – *Coxa*			
dvc	0.116342	0.993209	–0
dvc.a	0.918361	0.307682	–0.248888
dvc.1	–0.0771298	–0.740279	0.667861
dvc.2	0.0969571	–0.951354	–0.292447
dvc.3	–0.570192	–0.664354	0.483234
dvc.4	–0.847077	–0.527061	0.0683141
rot.trp	–0.494935	0.721271	–0.484569
pclx	–0.204936	0.410914	–0.888342
tcx	–0.400779	0.46028	–0.792161
tep	–0.364458	0.909327	–0.200735
rot.tr	–0.574732	0.682509	–0.451514
pct.1	–0.0149006	0.562357	0.82676
pct.2	–0.0166187	0.657161	0.753567
ret.cos	–0.530132	0.724382	–0.440716
ret.trt	–0.736613	–0.360531	–0.572205
ret.trs	–0.940583	–0.206462	–0.269588
pr.tr.co.a	–0.509809	0.791074	0.338076
pr.tr.co.b	–0.616198	0.775981	0.134737
pr.cot	–0.42265	–0.119699	0.898354
lev.tr.a	–0.84621	–0.503351	0.174832
lev.tr.b	–0.837664	–0.545907	0.0174566

Table 5 (continued)

Vectors *Coxa* – leg's tip			
pr.ta E	0.502567	–0.48553	0.715323
re.ti E	0.963132	–0.198949	0.181097
fl.ta E	0.938971	–0.343994	0.00129556
pr.ta.l E	0.998631	–0.0522638	0.0020519
fl.ti E	0.975734	0.202761	0.0826508
fl.un.p.fe E	0.998385	–0.0290651	–0.048817
fl.un.fe E	0.918645	–0.392973	0.0407781
dep.fe E	0.987645	0.155229	–0.02148
co.fe E	0.900243	0.433197	0.0436358
fl.un.tr E	0.886227	0.252777	0.388207
pr.fe E	0.54198	0.827951	–0.144067
co.fe	–0.93931	–0.334717	–0.0752432
re.ti.l	0.756539	–0.622999	0.198799
fl.ta	0.443163	–0.895865	–0.0321256
pr.ta.l	0.58615	–0.810203	–0
pr.ta	0.143604	–0.90963	0.38981
pr.fe	–0.801444	–0.576949	0.157536
fl.ti	0.987361	–0.131463	0.088521
fl.un.p.fe	0.857721	–0.511833	–0.048397
fl.un.tr	0.911329	–0.125008	0.39224
fl.un.fe	0.351922	–0.935886	–0.0163678
lev.tr.co	–0.436104	–0.870561	–0.227898
dep.fe	–0.997733	0.0255074	0.0622681
dep.tr	0.995114	0.0409365	0.0898499

Appendix D: Muscles vector direction cosine

Table 6 Muscles angle (radians)

Muscle	α	β	γ
Vectors *trunk* – *Coxa*			
dvc	1.45419	0.116606	1.5708
dvc.a	0.406878	1.25804	1.82233
dvc.1	1.648	2.40428	0.839466
dvc.2	1.47369	2.8284	1.86758
dvc.3	2.17754	2.29743	1.06645
dvc.4	2.58126	2.12593	1.50243
rot.trp	2.08856	0.76516	2.07667
pclx	1.77719	1.14734	2.66452
tcx	1.98316	1.09249	2.48514
tep	1.94385	0.429132	1.7729
rot.tr	2.18307	0.819607	2.03926
pct.1	1.5857	0.973563	0.597472
pct.2	1.58742	0.85375	0.717325
ret.cos	2.12955	0.760659	2.02719
ret.trt	2.39884	1.93963	2.17999
ret.trs	2.79514	1.77875	1.84376
pr.tr.co.a	2.10576	0.658233	1.22592
pr.tr.co.b	2.2347	0.682528	1.43565
pr.cot	2.00716	1.69078	0.454789
lev.tr.a	2.57963	2.09827	1.74653
lev.tr.b	2.56379	2.14827	1.58825

Table 6 (continued)

Muscle	α	β	γ
Vectors *Coxa* – leg's tip			
pr.ta E	1.04423	2.07777	2.36788
re.ti	0.272385	1.77108	1.7529
fl.ta E	0.35117	1.92196	1.57209
pr.ta.l E	0.0523279	1.62308	1.57285
fl.ti E	0.220748	1.36662	1.65354
fl.un.p.fe E	0.0568451	1.59987	1.52196
fl.un.fe E	0.406158	1.97466	1.61159
dep.fe E	0.157357	1.41494	1.54931
co.fe E	0.45047	1.12276	1.61445
fl.un.tr E	0.48166	1.31525	1.96948
pr.fe E	0.998005	0.595352	1.42623
co.fe	2.79141	1.9121	1.49548
re.ti.l	0.712792	2.24337	1.77093
fl.ta	1.11167	2.68117	1.53867
pr.ta.l	0.944498	2.51529	1.5708
pr.ta	1.42669	2.71319	1.97122
pr.fe	2.5005	2.18578	1.72899
fl.ti	0.159159	1.70264	1.65943
fl.un.p.fe	0.539976	2.10811	1.52238
fl.un.tr	0.424295	1.69613	1.97386
fl.un.fe	1.21117	2.78156	1.55443
lev.tr.co	2.02206	2.62714	1.34088
dep.fe	3.07425	1.54529	1.6331
dep.tr	0.0988972	1.52985	1.48083

Appendix E: Joints torque

Table 7 Muscles' torque $\left(\frac{gr \cdot mm^2}{s^2}\right)$

Muscle	τ_x	τ_y	τ_z
Stabilizers			
dvc	–12.8795	351.658	0
dvc.a	–100.102	106.922	20.6868
dvc.1	8.40724	–262.776	–47.3286
dvc.2	–11.2554	–345.311	20.7245
dvc.3	66.7127	–237.192	–34.2448
dvc.4	102.593	–189.861	–4.84115
$\sum$	53.47	–576.5	–45.00
Rotators			
rot.trp	34.0026	281.342	37.5341
pclx	17.7682	135.103	60.4408
tcx	36.752	155.517	34.3797
tep	30.87	325.304	10.7461
rot.tr	38.9101	263.355	33.4184
pct.1	1.21739	185.924	–42.1223
pct.2	1.35777	207.365	–40.412
$\sum$	160.88	1553.9	93.985
Retractors			
ret.cos	34.1522	274.549	33.8761
ret.trt	48.4823	–135.941	41.1221
ret.trs	60.0972	–77.8893	18.5655
$\sum$	142.73	60.719	93.564
Protractors			
pr.tr.co.a	39.0604	268.049	–23.9581
pr.tr.co.b	47.8748	263.671	–9.54829
pr.cot	33.1249	–40.0448	–63.6627
$\sum$	120.06	491.67	–97.16
Total	477.15	1529.7	45.376

Appendix F: Equivalent muscle model ℓ_ξ

From Figs. 7a-I-IV, the following functions describe elongations of the parallel/serial connections. The parallel muscles are assumed to elongate a same length, this work coupled parallel lengths by averaging them:

$$\ell_b = \frac{\ell_{b1} + \ell_{b2}}{2}, \tag{54a}$$

$$\ell_c = \frac{\ell_{c1} + \ell_{c2}}{2}, \tag{54b}$$

$$\ell_e = \frac{\ell_{e1} + \ell_{e2}}{2}, \tag{54c}$$

$$\ell_f = \frac{\ell_{f1} + \ell_{f2}}{2}, \tag{54d}$$

$$\ell_h = \frac{\ell_{h1} + \ell_{h2} + \ell_{h3}}{3}. \tag{54e}$$

Moreover, for Figs. 7-II-III, the following functions describe their elongations,

$$\ell_{eg} = \frac{\ell_{e1} + \ell_{e2}}{2} + \ell_g, \tag{55a}$$

the next equivalent muscle models, both ℓ_d and ℓ_{eg} are parallel,

$$\ell_{deg} = \frac{\ell_d + \ell_{eg}}{2}. \tag{55b}$$

The muscles interconnected in Delta configuration of Fig. 7-II are transformed into a Star configuration as shown in Fig. 7-III, hence their models are

$$\ell_{\epsilon_1} = \frac{\ell_b \ell_e}{\ell_b + \ell_e + \ell_f} \tag{56a}$$

and

$$\ell_{\epsilon_2} = \frac{\ell_b \ell_f}{\ell_b + \ell_e + \ell_f} \tag{56b}$$

and

$$\ell_{\epsilon_3} = \frac{\ell_e \ell_f}{\ell_b + \ell_e + \ell_f} \tag{56c}$$

Finally, the equivalent model ℓ_ξ shown in Fig. 7-IV is obtained by modeling the serial connection of ℓ_{ϵ_2} and ℓ_{deg}, which are in parallel with the serial connection between ℓ_{ϵ_3} and ℓ_h, such that

$$\ell_\xi = \ell_{\epsilon_1} + \frac{\ell_{\epsilon_2} + \ell_{deg} + \ell_{\epsilon_3} + \ell_h}{2} \tag{57a}$$

by reordering and expanding fractional terms,

$$\ell_\xi = \ell_{\epsilon_1} + \frac{\ell_{\epsilon_2} + \ell_{\epsilon_3}}{2} + \frac{\ell_{deg} + \ell_h}{2} \tag{57b}$$

by substituting each term's formula,

$$\begin{aligned} \ell_\xi = & \frac{\ell_b \ell_e}{\ell_b + \ell_e + \ell_f} + \frac{1}{2}\left(\frac{\ell_b \ell_f}{\ell_b + \ell_e + \ell_f} + \frac{\ell_e \ell_f}{\ell_b + \ell_e + \ell_f}\right) + \\ & \frac{1}{2}\left(\frac{\ell_d}{2} + \frac{\ell_{e_1} + \ell_{e_2}}{2} + \ell_g + \ell_h\right). \end{aligned} \tag{57c}$$

To simplify notation, let us define $\ell_\alpha \doteq \ell_b + \ell_e + \ell_f$, algebraically substitute and arrange to obtain a complete function in terms of muscles' length,

$$\ell_\xi = \frac{2\ell_b \ell_e + \ell_b \ell_f + \ell_e \ell_f}{2\ell_\alpha} + \frac{\ell_d + \ell_{e_1} + \ell_{e_2} + 2\ell_g + 2\ell_h}{4}. \tag{57d}$$

Supplementary Information The online version contains supplementary material available at (https://doi.org/10.1007/s12213-021-00141-y).

References

1. Spröwitz A, Göttler C, Sinha A, Caer C, Öoztekin MU, Petersen K, Sitti M, Scalable pneumatic and tendon driven robotic joint inspired by jumping spiders (2017). In: 2017 IEEE Intl. conf. on robotics and automation, Singapore, 2017, pp 64–70. https://doi.org/10.1109/ICRA.2017.7988692
2. Donatelli CM, Bradner SA, Mathews J, Sanders E, Culligan C, Kaplan D, Tytell ED (2018) Prototype of a fish inspired swimming silk robot. In: 2018 IEEE Intl. conf. on soft robotics, Livorno, pp 60–65. https://doi.org/10.1109/ROBOSOFT.2018.8404897
3. Li D, Zeng Z, Cao J, Lu D, Xiong C, Lian L (2016) A bio-inspired underwater glider with undulatory fin for long-duration, spatially explicit water column sampling. In: 2016 IEEE/OES autonomous underwater vehicles, Tokyo, pp 62–68. https://doi.org/10.1109/AUV.2016.7778722
4. Fras J, Noh Y, Macias M, Wurdemann H, Althoefer K (2018) Bio-Inspired Octopus robot based on novel soft fluidic actuator. In: 2018 IEEE Intl. conf. on robotics and automation, brisbane, QLD, pp 1583–1588. https://doi.org/10.1109/ICRA.2018.8460629
5. Kang R, Guglielmino E, Branson DT, Caldwell DG (2012) Bio-inspired crawling locomotion of a multi-arm octopus-like continuum system. In: 2012 IEEE/RSJ Intl. conf. on intelligent robots and systems, Vilamoura, pp 145–150. https://doi.org/10.1109/IROS.2012.6385954
6. Li G, Deng Y, Osen OL, Bi S, Zhang H (2016) A bio-inspired swimming robot for marine aquaculture applications: From concept-design to simulation, OCEANS 2016, Shanghai 1–7. https://doi.org/10.1109/OCEANSAP.2016.7485691
7. Park HS, Sitti M (2009) Compliant footpad design analysis for a bio-inspired quadruped amphibious robot. In: 2009 IEEE/RSJ intl. conf. on intelligent robots and systems, St Louis, MO, pp 645–651. https://doi.org/10.1109/IROS.2009.5354680
8. Yamada Y, Nakamura T (2018) Blade-Type Crawler capable of running on the surface of water as Bio-Inspired by a basilisk lizard. In: 2018 IEEE/RSJ intl. conf. on intelligent robots and systems, Madrid, pp 1–9. https://doi.org/10.1109/IROS.2018.8594397
9. Wang Z, Dai Z, Yu Z, Shen D (2014) Optimal attaching and detaching trajectory for bio-inspired climbing robot using dry adhesive. In: 2014 IEEE/ASME intl. conf. on advanced intelligent mechatronics, Besacon, pp 990–993. https://doi.org/10.1109/AIM.2014.6878209
10. Park SH, Hong DP (2013) Optimal bio-inspired structure of a quadruped by the method of energy efficiency, IEEE ISR 2013, Seoul, 1–4. https://doi.org/10.1109/ISR.2013.6695653
11. Billah MM, Khan MR (2015) Bio-inspired snake robot locomotion: A CPG-based control approach. In: 2015 5th National symp. on information tech.: towards new smart world, Riyadh, pp 1–6. https://doi.org/10.1109/NSITNSW.2015.7176385
12. Su X, Gao J, Zhao Z, Wu Q, Huang C (2012) Structural analysis and design of round belt drive snake-like robot. In: IET Intl conf. on information science and control engineering 2012, Shenzhen, pp 1–5. https://doi.org/10.1049/cp.2012.2299
13. Zhang J, Cheng B, Yao B, Deng X (2015) Adaptive robust wing trajectory control and force generation of flapping wing MAV. In: 2015 IEEE Intl. conf. on robotics and autom., Seattle, Washington, May 26-30, pp 5852–5857
14. Harvey N, Nel AL (2015) Arachnid-inspired kinesthesia for legged robots. In: Pattern recognition association of south africa and robotics and mechatronics intl. conf., port elizabeth, pp 245–251. https://doi.org/10.1109/RoboMech.2015.7359530, p 2015
15. Martínez-García EA, Torres-Mendez LA, Mohan RE (2014) Multi-legged robot dynamics navigation model with optical flow. Intl J of Intell Unmanned Syst 2(2):121–139. Emerald. https://doi.org/10.1108/IJIUS-04-2014-0003
16. Jamisola RS, Mastalli C (2017) Bio-inspired holistic control through modular relative Jacobian for combined four-arm robots. In: 2017 18th intl. conf. on advanced robotics, Hong Kong, pp 346–352. https://doi.org/10.1109/ICAR.2017.8023631
17. Ishigaki Y, Ito K (2014) Proposal for semiautonomous centipede-like robot for rubble - development of an actual scale robot and validation of its mobility. In: Proc. of the 2014 intl. conf. on advanced mechatronic systems, Kumamoto, 409–414. https://doi.org/10.1109/ICAMechS.2014.6911580
18. Masuda M, Ito K (2014) Semi-autonomous centipede-like robot with flexible legs. In: 2014 IEEE Intl. symposium on safety, security, and rescue robotics, Hokkaido, pp 1–6. https://doi.org/10.1109/SSRR.2014.7017667
19. Yasui K, Sakai K, Kano T, Owaki D, Ishiguro A (2017) Decentralized control scheme for myriapod robot inspired by adaptive and resilient centipede locomotion. PLoS ONE 12(2):1–12
20. Shinya A, Takahiro T, Solchiro F, Tetsuro F, Kei S, Kazuo T (2016) Kyoto University, "Advantage of straight walk instability in turning maneuver of multilegged locomotion: a robotics approach". [Online]. Available: https://doi.org/10.1038/srep30199
21. Geijtenbeek T, van de Panne M, van der Stappen AF (2013) Flexible muscle-based locomotion for bipedal creatures, ACM Trans. on Graphics, 32(206)
22. Inagaki S, Niwa T, Suzuki T (2010) Follow-the-contact-point gait control of centipede-like multi-legged robot to navigate and walk

on uneven terrain. In: The 2010 IEEE/RSJ intl. conf. on intelligent robots and systems, Taiwan, pp 5331–5346

23. Chen J, Liu Y, Zhao J, Zhang H, Jin H (2014) Biomimetic design and optimal swing of a hexapod robot leg. J of Bionic Eng 11(1):26–35
24. Siriwut W, Edgecombe GD, Sutcharit C, Tongkerd P, Panha S (2016) A taxonomic review of the centipede genus Scolopendra Linnaeus, 1758 (Scolopendromorpha, Scolopendridae) in mainland Southeast Asia, with description of a new species from Laos. ZooKeys 590:1–124. https://doi.org/10.3897/zookeys.590.7950
25. Koch LE (1983) Revision of the australian centipedes of the genus cormocephalus newport (chilopoda: Scolopendridae: Scolopendrinae). Aust J Zool 31:799–833
26. Manton SM (1965) Functional requirements and body design in Chilopoda. In: The evolution of arthropodan locomotory mechanisms, Part 8, J. of the Linnean Society of London, vol 45. Blackwell Pub, pp 251-484
27. Lewis J (1981) The musculature and endoskeleton. In: The biology of centipedes. Cambridge University Press, Cambridge, pp 67-84. https://doi.org/10.1017/CBO9780511565649.005
28. Gasser HS, Hill AV (1924) The dynamics of muscular contraction, Proc. of the Royal Society of London. Series B, 96(678)
29. Full J, Kubow T, Schmitt J, Holmes P, Koditschek D (2002) Quantifying dynamic stability and maneuverability in legged locomotion. Integr Comp Biol 42(1):149–157
30. Jäntsch M, Schmaler C, Wittmeier S, Dalamagkidis K, Knoll A (2011) A scalable joint-space controller for musculoskeletal robots with spherical joints. In: 2011 IEEE intl. conf. on robotics and biomimetics, Karon Beach, Phuket, pp 2211–2216
31. Wang J, Hammer S, Delp S, Koltun V (2012) Optimizing locomotion controllers using biologically-based actuators and objectives. ACM Trans Graph 31(4):1–11
32. Kuroda S, Uchida N, Nakagaki T (2018) Dynamic gait transition in the Scolopendromorpha scolopocryptops rubiginosus L. Koch centipede, Cold Spring Harbor Laboratory. https://doi.org/10.1101/312280
33. Yasui K, Kano T, Standen EM et al (2019) Decoding the essential interplay between central and peripheral control in adaptive locomotion of amphibious centipedes. Sci Rep 9:18288. https://doi.org/10.1038/s41598-019-53258-3